

RELATED PROGENITOR MODELS FOR LONG-DURATION GAMMA RAY BURSTS AND TYPE IC SUPERLUMINOUS SUPERNOVAE

DAVID R. AGUILERA-DENA,¹ NORBERT LANGER,^{1,2} TAKASHI J. MORIYA,³ AND ABEL SCHOOTEMEIJER¹

¹*Argelander-Institut für Astronomie, Universität Bonn, Auf dem Hügel 71, 53121 Bonn, Germany*

²*Max-Planck-Institut für Radioastronomie, Auf dem Hügel 69, 53121 Bonn, Germany*

³*Division of Theoretical Astronomy, National Astronomical Observatory of Japan, National Institutes for Natural Sciences, 2-21-1 Osawa, Mitaka, Tokyo 181-8588, Japan*

ABSTRACT

We model the late evolution and mass loss history of rapidly rotating Wolf-Rayet stars in the mass range $5 M_{\odot} \dots 100 M_{\odot}$. We find that quasi-chemically homogeneously evolving single stars computed with enhanced mixing retain very little or no helium and are compatible with Type Ic supernovae. The more efficient removal of core angular momentum and the expected smaller compact object mass in our lower mass models lead to core spins in the range suggested for magnetar driven superluminous supernovae. Our more massive models retain larger specific core angular momenta, expected for long-duration gamma-ray bursts in the collapsar scenario. Due to the absence of a significant He envelope, the rapidly increasing neutrino emission after core helium exhaustion leads to an accelerated contraction of the whole star, inducing a strong spin-up, and centrifugally driven mass loss at rates of up to $10^{-2} M_{\odot} \text{ yr}^{-1}$ in the last years to decades before core collapse. Since the angular momentum transport in our lower mass models enhances the envelope spin-up, they show the largest relative amounts of centrifugally enforced mass loss, i.e., up to 25% of the expected ejecta mass. Our most massive models evolve into the pulsational pair-instability regime. We would thus expect signatures of interaction with a C/O-rich circumstellar medium for Type Ic superluminous supernovae with ejecta masses below $\sim 10 M_{\odot}$ and for the most massive engine-driven explosions with ejecta masses above $\sim 30 M_{\odot}$. Signs of such interaction should be observable at early epochs of the supernova explosion, and may be related to bumps observed in the light curves of superluminous supernovae, or to the massive circumstellar CO-shell proposed for Type Ic superluminous supernova Gaia16apd.

Keywords: stars: massive — stars: mass-loss — supernovae: general — circumstellar medium

arXiv:1804.07317v1 [astro-ph.SR] 19 Apr 2018

1. INTRODUCTION

With the advent of multi-wavelength, all-sky surveys dedicated to observing the onset and aftermath of transient astrophysical events such as supernovae (SNe) and gamma-ray bursts (GRBs), and the fast follow-up observations carried out by space-based and ground instruments, our understanding of the properties of their progenitors and environments has dramatically increased in the last decades (e.g., [Rau et al. 2009](#); [Drake et al. 2009](#); [Kaiser et al. 2010](#); [Flaugher et al. 2015](#); [Tanaka et al. 2016](#)). As observations become more numerous and have higher resolution and time coverage, it becomes possible to refine our theoretical understanding of the environment and physical conditions that led to these events.

The large increase in the number of observed SNe and the improvement in the analysis techniques has also led to identify new classes of SNe, well beyond the classical Types Ia, Ib, Ic, and II. In particular, two of these new classes are currently thought to be caused by rapidly rotating H- and He-poor massive progenitor stars, the broad-lined Type Ic SNe (SNe Ic-bl, also known as hypernovae, HNe), and the superluminous Type Ic SNe (SLSNe-Ic). A fraction of the SNe Ic-bl is observationally associated with long-duration gamma-ray bursts (IGRBs) ([Modjaz et al. 2016](#)), which have been suggested to be triggered by the formation of rapidly rotating accreting black holes in the collapsar scenario ([Woosley 1993](#)), or by formation of rapidly spinning super-magnetic neutron stars in the magnetar scenario ([Usov 1992](#); [Woosley 2010](#)). While conceivably all IGRBs are associated with the supernova explosion of a rapidly rotating Wolf-Rayet star, not all SNe Ic-bl appear to be associated with an IGRB ([Fynbo et al. 2006](#); [Gehrels et al. 2006](#); [Della Valle et al. 2006](#); [Gal-Yam et al. 2006](#)). Nevertheless, their large explosion energies and large-scale asphericity ([Nomoto et al. 2010](#)) demand an explosion mechanism other than that of ordinary core-collapse SNe, which might be provided by the formation of a central rapidly rotating compact object.

Whereas detailed progenitor evolution models for SLSNe-Ic are yet to be developed, [Nicholl et al. \(2017b\)](#), based on the analysis of a large sample of observed SLSNe, suggest that they may be products of chemically homogeneous evolution, or were spun up through binary interaction. It appears that the magnetar scenario can explain the required large energy on timescales of weeks as being tapped from the rotational energy of a millisecond magnetar ([Kasen & Bildsten 2010](#); [Woosley 2010](#)). Energy input on these timescales is provided in ordinary supernovae through the decay of radioactive nickel. However, the large amounts of nickel required to explain the peak brightness appears to be incompatible with many Type Ic SLSN observations (e.g., [Inserra et al. 2013](#); [Nicholl et al. 2013](#)). Whereas the necessary B-field in this case is somewhat smaller than the one needed to produce IGRBs ([Metzger et al. 2015](#); [Margalit et al. 2018](#)) also here a nearly critically rotating Wolf-Rayet star is indispensable for producing the magnetar at core collapse.

Several studies have accounted for the effect of rotation in massive star evolution models, highlighting its impact on

observable stellar properties, including the possible consequences that the high rotation rate may have for the ultimate fate of the star ([Heger et al. 2000](#); [Ekström et al. 2012](#); [Georgy et al. 2012, 2013](#); [Yoon et al. 2006](#); [Brott et al. 2011](#); [Chatzopoulos & Wheeler 2012a](#); [Szécsi et al. 2015](#)). In particular, chemically homogeneous evolution (CHE) due to rotationally induced mixing, which is favoured to occur at low metallicities, has been suggested to lead to the formation of IGRBs ([Yoon & Langer 2005](#); [Woosley & Heger 2006](#)), but also various close binary evolution channels have been suggested to produce rapidly rotating Wolf-Rayet stars at core collapse leading to IGRBs and SNe Ic-bl ([Detmers et al. 2008](#); [Podsiadlowski et al. 2010](#)).

In this paper, we investigate the pre-collapse evolution of rapidly rotating stars devoid of H, with an emphasis on the structural changes which occur after core He exhaustion. In [Sect. 2](#) we describe the method we used to compute our stellar evolution sequences, and the assumptions that go into our calculations. In [Sect. 3](#) we present our results, while in [Sect. 4](#) we present possibly observable consequences of our findings in SNe. We end the paper with a brief discussion in [Sect. 5](#) before presenting our conclusions in [Sect. 6](#).

2. METHOD

We performed evolutionary calculations of rotating massive stars using the Modules for Experiments in Stellar Astrophysics (MESA) code—in its version r10000—which includes the effects of stellar rotation ([Paxton et al. 2011, 2013, 2015, 2017](#)). Our initial models have uniform composition, and a metallicity of $Z = 0.00034$, or $\sim 1/50 Z_{\odot}$, scaled from solar metallicity ([Grevesse et al. 1996](#)), and an initial helium mass fraction of $Y=0.2477$ ([Peimbert et al. 2007](#)). While this metallicity does not represent the average of the observed SLSNe Ic population, it was chosen to avoid drastic spin-down and maximize the effects obtained from rotationally induced chemically homogeneous evolution. We provide a discussion of the consequences of our choice in [Sect. 5](#).

The initial masses of the evolutionary sequences we discuss are between 5 and 100 M_{\odot} , and they have initial rotational velocity of 600 km/s, which corresponds to a fraction of their critical rotation rate in the range of 0.68 to 0.89. This velocity corresponds to that of the fastest rotating known O star ([Ramírez-Agudelo et al. 2013](#)), and is chosen such that rotationally induced chemically homogeneous evolution is guaranteed ([Yoon et al. 2006](#)). The calculations are started from models of uniformly rotating pre-main sequence stars, and are continued until at least core carbon depletion, and up to the formation of an iron core in most cases. Models above $\sim 50M_{\odot}$ may evolve until the onset of the pulsational pair instability ([Woosley 2017](#)). We used the nuclear network `approx21` included in MESA.

Convection is modelled with the standard mixing length theory ([Böhm-Vitense 1958](#)), using $\alpha_{ML} = 1.5$. We adopt the Ledoux criterion for convective instability, and apply semi-convective mixing with an efficiency factor of $\alpha_{SC} = 0.01$ ([Langer 1991](#)). Convective overshooting is applied by us-

ing a step function, with $\alpha_{ov} = 0.335$ following [Brott et al. \(2011\)](#).

We compute two sets of models, using different efficiency parameters for rotational mixing. In our first set (the A Series), we adopt the following parameters: Our treatment of mixing includes Eddington-Sweet circulations, secular and dynamical instability, and the Goldreich-Schubert-Fricke instability, with an efficiency factor of $f_c = 1/30$ following [Brott et al. \(2011\)](#). We employ the Tayler-Spruit dynamo to compute the internal magnetic field strength and the corresponding transport of angular momentum as described in and [Heger et al. \(2005\)](#). Time smoothing of the mixing coefficients is included to make our results consistent with those of [Szécsi et al. \(2015\)](#).

In our second set of models (the B Series), we enhance the diffusion coefficient due to rotational mixing by a factor of ten. While such high rotational mixing efficiency may lead to too strong mixing of nitrogen in slowly and moderately rotating O stars ([Brott et al. 2011](#)), we use it here as a tool to produce rapidly rotating progenitor models which are suitable to explain Type Ic supernovae. While it can not be excluded that at very high rotation rates, non-linear effects lead to a stronger dependence of the mixing efficiency on the rotation rate than at moderate or slow rotation, we argue below that in any case, our major results are merely independent of how a rapidly rotating SN Ic progenitor model has actually been produced.

Mass loss rates for H rich (with a surface H mass fraction $X_S > 0.7$) and for H poor models ($X_S < 0.4$), were computed following [Vink et al. \(2001\)](#) and [Hamann et al. \(1995\)](#), respectively, the latter multiplied by a factor of 1/10 to account for subsequent calibrations (cf. Fig. 1 of [Yoon & Langer 2005](#)), and both using a metallicity scaling of $\dot{M} \sim (Z/Z_\odot)^{0.85}$. For intermediate surface H abundances we smoothly interpolate between the two, as in [Marchant et al. \(2016\)](#) and [Yoon et al. \(2006\)](#). We apply a mass loss enhancement based on the ratio of the rotation rate at the stellar surface to the critical rotation rate

$$\Omega_{crit} = \sqrt{\frac{GM}{R^3}(1-\Gamma)}, \quad (1)$$

where $\Gamma = L/L_{Edd}$ is the ratio of the luminosity of the star to its Eddington luminosity; as

$$\dot{M}(\Omega) = \dot{M}(0) \left(\frac{1}{1 - \frac{\Omega}{\Omega_{crit}}} \right)^\xi, \quad (2)$$

where $\xi = 0.43$ ([Friend & Abbott 1986](#); [Bjorkman & Cassinelli 1993](#)). Models with Ω/Ω_{crit} approaching unity lead to the divergence of \dot{M} according to Eq. 2. To work around this, we set the maximum value for Ω/Ω_{crit} to 0.98, calculating the mass loss rate implicitly when this limit was exceeded, such that over-critical rotation and diverging mass loss rates are avoided. We note that the resulting mass loss rate is well defined and insensitive to the chosen threshold value ([Langer 1998](#)).

The details of our mass loss enhancement procedure are to a large part chosen to facilitate numerical convergence, but do not affect our main results. Its practical purpose is to determine the amount of mass loss which is required for the star to not exceed the limit of critical rotation. As the radiation driven winds of our low metallicity models are weak, this amount is determined simply by the initial conditions of the models, and the structural changes imposed by the internal stellar evolution.

3. MODEL PROPERTIES

The observed dependence of the stellar wind mass loss rate on metallicity ([Mokiem et al. 2007](#)) implies that metal poor stars lose little mass during their evolution. However, in rapid rotators, centrifugally driven mass loss may cause high mass loss rates even at low metallicity during overall contraction stages that occurs between major nuclear burning stages ([Yoon et al. 2006](#); [Ekström et al. 2008](#)). Such events will heavily affect the circumstellar medium (CSM) structure of such stars ([van Marle et al. 2008](#)), which may lead to different pre-SN configurations in different circumstances.

To investigate this, we perform evolutionary calculations for rapidly rotating stars in the initial mass range from 5 to 100 M_\odot , which undergo CHE. Our Series A models follow closely the paths described by ([Yoon et al. 2006](#)) and [Szécsi et al. \(2015\)](#), and we describe them below for comparison. However, many of these models retain massive helium-rich envelopes and might thus correspond to progenitors of Type Ib supernovae. We therefore focus below on our Series B models, in which the rotational mixing remains strong enough during core helium burning such that little helium remains. As we shall see, this does not only affect the spectroscopic type of the potentially produced SNe, but it profoundly changes the evolution of the internal angular momentum and of the CSM.

3.1. Evolution of the internal chemical structure

As described in Sect. 2, our initial models have a uniform composition, and they evolve quasi-chemically homogeneously throughout core H burning. As they transition to core He burning, they contract, and a significant rotationally enhanced mass loss occurs (see Sect. 3.4). As illustrated in Figs. 1 and 2, H is essentially absent at the pre-SN stage in all our models, regardless of their mass. This is due in part to the mixing that brings most of the H into the core, and also to the rotationally enhanced mass loss that removes the remaining H from the surface.

In our Series A models, the extent of the region where mixing is efficient, and the amount of mass lost during contraction determine whether a particular evolutionary sequence remains quasi-chemically homogeneous throughout He burning, or instead develops a core-envelope structure in this phase. Two models from Series A sequences shown in Fig. 1 illustrate the two different cases: models below $\sim 20 M_\odot$ retain He-rich envelopes until after core He burning, and ignite a vigorous helium shell burning. More massive models produce less massive helium envelopes, with helium nearly

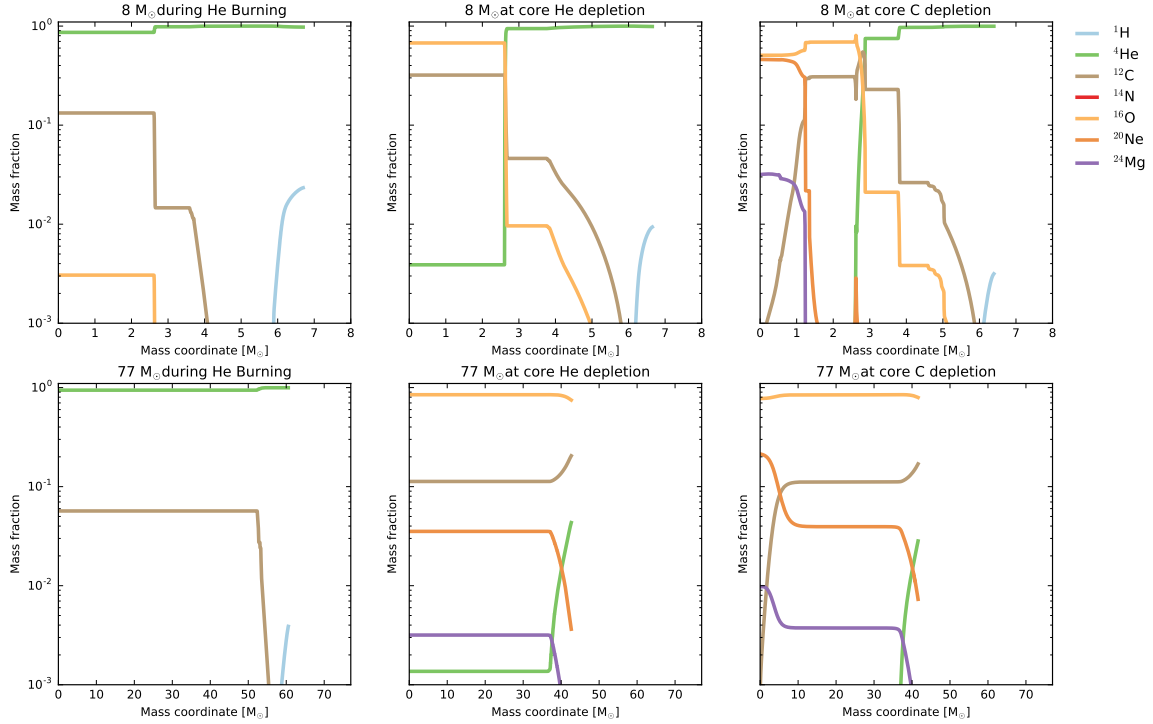


Figure 1. Mass fractions of the major chemical elements as function of the Langrangian mass coordinate in stellar models from two evolutionary sequences of the A Series at three different times, during core He burning, at He core depletion, and at C core depletion.

absent in the highest masses (cf., Tab. 2). He-shell burning is weak or absent in these models, and has no significant effect.

Our Series B models retain little helium ($< 0.06 M_{\odot}$) regardless of the initial mass (see Fig. 2 and Tab. 1). These models do not develop a core-envelope structure and remain well mixed also during He burning. None of these models develops significant He-shell burning.

3.2. Core contraction and envelope expansion

As all massive star models, our models experience an overall contraction immediately after core H exhaustion (Fig. 3). While in the stellar core, this contraction continues until core helium ignition, the ignition of a powerful H shell source stops the contraction of the envelope and leads to its rapid expansion in stellar models which follow ordinary evolution (cf. Brott et al. 2011).

In our models, which experience CHE, the latter effect is weak or absent. Since little H is left at core H exhaustion in our massive models ($M > 20 M_{\odot}$; see Sect. 3.1), burning in their H shells is weak, and they show no expansion at this stage. Our lowest mass models of the A Series do experience a H-shell driven expansion (at $T_c \simeq 10^8$ K; see Fig. 4). However, most of their remaining H is quickly lost due to rotationally enhanced mass loss (Sect. 3.4) and H-shell burning, such that their envelopes contract soon thereafter. During core helium burning ($T_c \simeq 10^8$ K), the radii of all the models correspond well to the mass-radius relation of helium stars (Langer 1989).

Most remarkably, Fig. 3 shows a pronounced dichotomy in the final radius evolution of our models. Whereas the three

lower mass Series A models strongly expand after core helium exhaustion, all other models continue to contract.

The expansion of the lower mass Series A models is driven by the onset of strong helium shell burning. As shown in Fig. 4 (top) at the example of our $8 M_{\odot}$ model, the final radius increase in this sequence starts about one thermal timescale after the onset of helium shell burning.

Fig. 4 (middle) shows, again with our $8 M_{\odot}$ model as an example, why this expansion does not occur in our Series B models. The reason is that they contain much less helium in their envelopes at this stage, such that the helium shell source is much weaker or absent. Therefore, even the lower mass models of Series B contract as a whole after core helium exhaustion. The contracting models end their lives as very compact and extremely hot stars, with $T_{\text{eff}} \simeq 150\,000 \dots 300\,000$ K (cf. Tables 1 and 2).

Fig. 4 also shows why the massive models of Series A do not expand after core helium exhaustion. The amount of helium in the $39 M_{\odot}$ model at this stage is still large ($\sim 4 M_{\odot}$; cf., Tab. 2), and as shown in the figure, the energy production in the helium shell source exceeds the stellar luminosity by far at some point. However, due to the copious neutrino emission in the stellar core, the remaining life time of the model at this stage is significantly smaller than its Kelvin-Helmholtz timescale. It undergoes the post-core helium exhaustion overall contraction, and reaches core collapse before the helium shell burning can expand the envelope.

From Fig. 5, we can understand the timescale of the radius change of our models, by comparing it to various other timescales. As expected, during core H and core helium

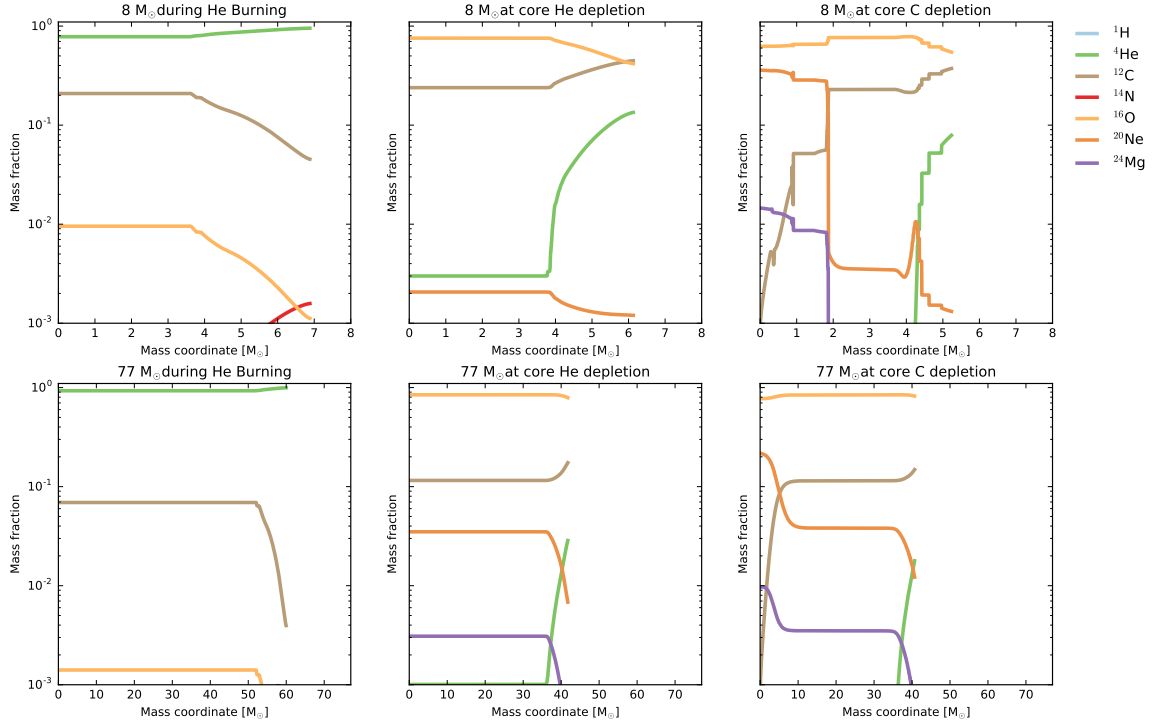


Figure 2. As Figure 1, but for the corresponding models from the B Series.

burning, the stellar radius changes on the nuclear timescale (not shown). This is 2 to 3 orders of magnitude larger than the Kelvin-Helmholtz timescale

$$\tau_{\text{KH}} = \frac{GM^2}{RL}, \quad (3)$$

on which the stellar radius changes at core H exhaustion. However, those models which contract after core helium exhaustion do so on a much shorter timescale. With the neutrino-mediated Kelvin-Helmholtz timescale defined as

$$\tau_{\text{KH},\nu} = \frac{GM^2}{R(L+L_\nu)}, \quad (4)$$

where L_ν is the neutrino luminosity, Fig. 5 shows that the contraction occurs on this timescale. Therefore, on one hand, these models, which are essentially just bare C/O-cores, contract to compensate for their neutrino losses.

On the other hand, the top panel of Fig. 5 shows that our $8 M_\odot$ Series A model performs its final expansion on the ordinary Kelvin-Helmholtz timescale, even though its C/O-core also contracts on the neutrino-mediated Kelvin-Helmholtz timescale. This demonstrates that only contraction can be accelerated by neutrino losses, but evidently expansion can not, since the neutrinos do not contribute to the pressure inside the star.

Therefore, even if the core contraction leads to the ignition of a vigorous helium shell source (as it is the case in our $39 M_\odot$ sequence; cf. Fig. 4), but the time to core collapse is significantly shorter than the ordinary Kelvin-Helmholtz timescale, the star will not be able to expand any more. Con-

sequently, our $39 M_\odot$ model decreases its radius monotonically as function of time until it reaches a minimum, at which it stays until the end of our calculations (Fig. 3).

We note that during the pre-collapse evolution of ordinary red supergiants, the cores after core helium exhaustion must contract on the neutrino-mediated Kelvin-Helmholtz timescale. As a consequence, in all of them a vigorous helium shell burning will start. Whether or not this will give rise to a subsequent stellar expansion will again depend on the mass of the star. For the highest masses, the core contraction timescale will be smaller than the stellar Kelvin-Helmholtz timescale, and no expansion will occur. For lower masses, in particular when core degeneracy slows down the core contraction, the envelope has ample time to expand, and the stellar track will climb up the Hayashi line in the HR diagram (see e.g. Fig. 1 of Georgy et al. 2012).

3.3. Evolution of the internal angular momentum distribution

The distribution of angular momentum in our evolutionary models initially corresponds to uniform rotation. Its evolution is calculated by considering the combined effects of hydrodynamic and magnetic angular momentum transport, and angular momentum loss due to mass loss. In particular, the Spruit-Taylor mechanism, which has been invoked to explain the observed slow rotation rates of white dwarfs (Suijs et al. 2008) and young pulsars (Heger et al. 2005), can efficiently transport angular momentum from the core into the envelope of our models.

Figure 6 shows the distribution of angular momentum in the stellar interior in several stages of evolution, for selected

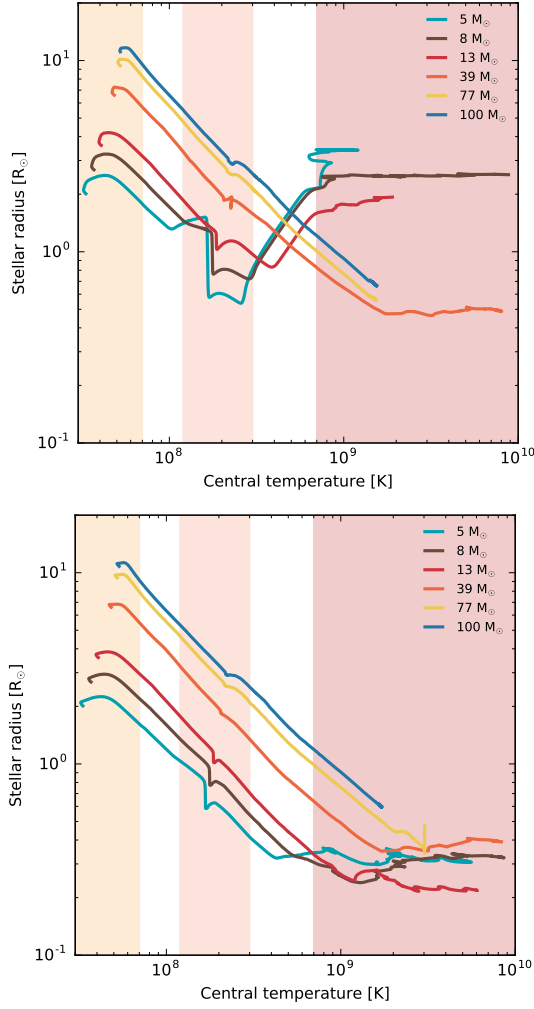


Figure 3. Stellar radius as a function of central temperature for the evolutionary sequences of Series A (top) and Series B (bottom). The temperature ranges of core H, He and heavy element burning are shaded.

models. We show this following Suijs et al. (2008), by plotting the total angular momentum enclosed inside a given mass coordinate m , divided by $m^{5/3}$; namely $(m)^{-5/3}J(m) = (m)^{-5/3} \int_0^m j(m')dm'$, where $j(m')$ is the specific angular momentum at mass coordinate m' . A uniformly rotating sphere of constant density will have flat profile in this diagram.

Figure 6 shows that in the lower mass models ($5 \dots 20 M_{\odot}$), a significant amount of angular momentum transport occurs after core helium exhaustion. This increases the specific angular momentum in the envelope, and therefore, at a given radius, the surface rotation of the models. In the lower mass models, this effect leads to an enhancement of the rotationally induced mass loss despite their expansion (see Sect. 3.4).

In the more massive models, the short core contraction timescale does not allow for significant angular momentum transport after core helium exhaustion. The angular momentum distribution remains almost frozen-in. Therefore, even

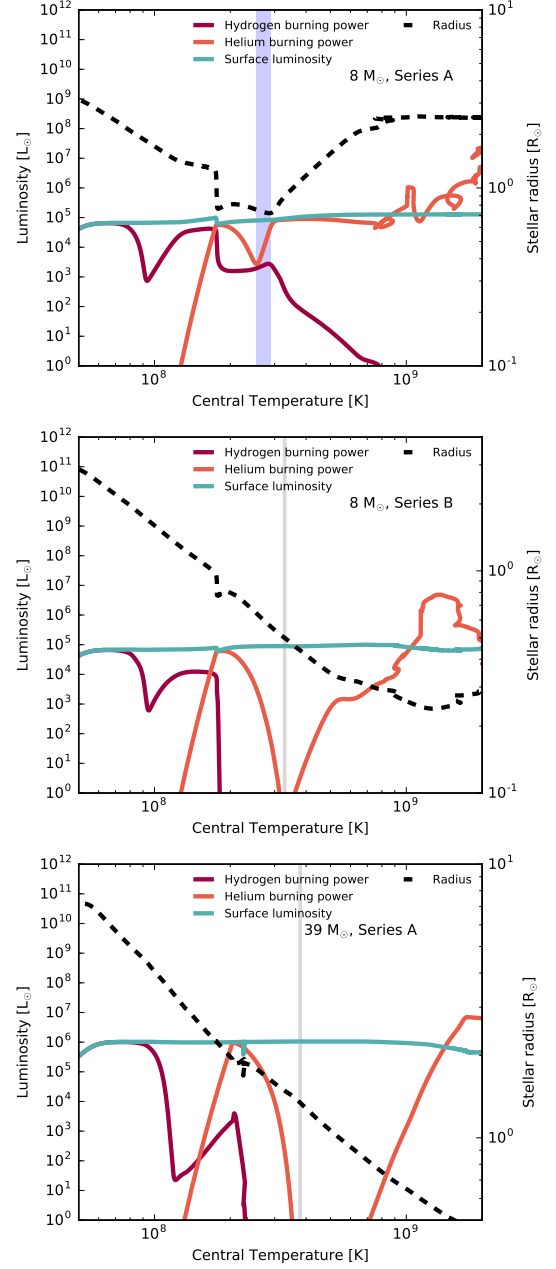


Figure 4. Nuclear energy produced per second by H and helium burning, surface luminosity (solid lines, left axis), and stellar radius (dashed line, right axis), as a function of central temperature, for the $8 M_{\odot}$ (top) and $39 M_{\odot}$ sequences (bottom) from Series A. The blue highlighted region corresponds to the duration of one Kelvin-Helmholtz timescale beginning at He shell ignition in the top panel. Bottom panels show instead the temperature of shell ignition, but the remaining lifetime is shorter than the Kelvin-Helmholtz timescale at this point.

though the wind induced amount of mass lost by the massive stars is larger, their final specific core angular momentum is larger than that of the lower mass models. This is illustrated

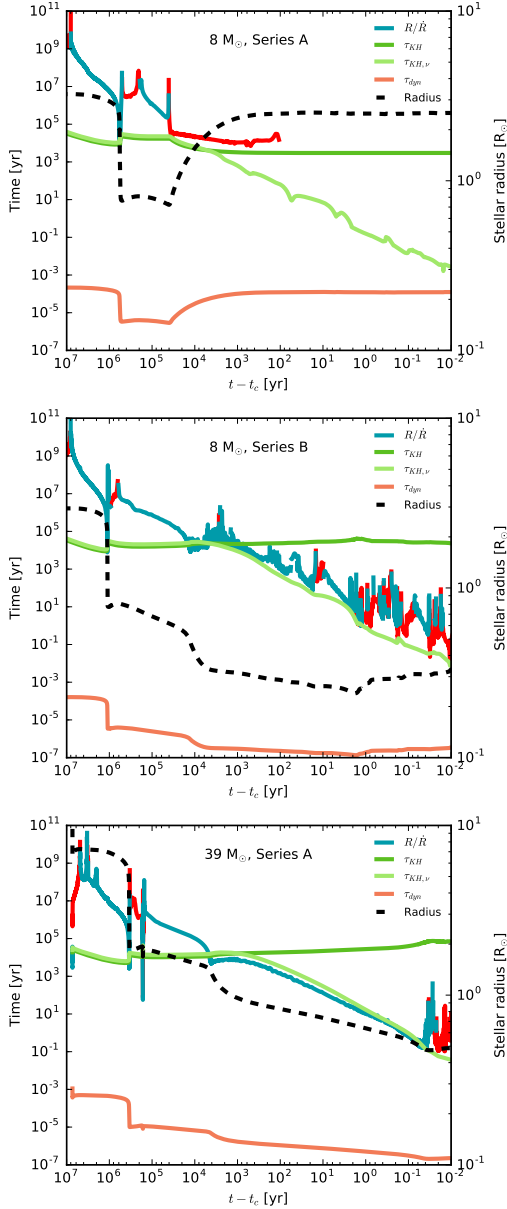


Figure 5. Time-scale of the radius evolution R/\dot{R} (in blue for contraction, in red for expansion), Kelvin-Helmholtz time-scale τ_{KH} (Eq. 3), neutrino-mediated thermal time-scale $\tau_{KH,\nu}$ (Eq. 4), and dynamical time-scale τ_{dyn} as a function of the remaining time to core collapse, for the $8 M_{\odot}$ models of Series A (top) and Series B (middle), and for the $39 M_{\odot}$ model of Series A (bottom). Parts of the R/\dot{R} line are omitted as the radius (black dashed line) becomes almost constant, and numerical noise dominates due to small changes of the radius.

in Fig. 7, which shows the time evolution of the average specific angular momentum of the core.

In Tabs. 1 and 2, we provide the final core specific angular momentum of our models, and estimate the initial spin period of a potential neutron star emerging from the collapsing core.

The obtained results for Series A agree qualitatively with the lowest metallicity models of Yoon et al. (2006).

The cores of the low mass models of Series A appear to rotate too slowly to apply either, the magnetar or the collapsar scenario to them. Due to the core-envelope structure established during core helium burning, the expanding helium envelope produces a strong braking of the core rotation after core-helium exhaustion. The cores of the massive models retain sufficient angular momentum to qualify for the collapsar scenario, but only the most massive models die with less than one solar mass of helium left in their envelopes.

Our Series B models are all essentially helium-free at the time of collapse, and all of them have average specific core angular momenta of more than $10^{15} \text{ cm}^2 \text{ s}^{-1}$. Certainly the $5 M_{\odot}$ and $8 M_{\odot}$ sequences, with final masses of $3.4 M_{\odot}$ and $5.2 M_{\odot}$, and possibly also the $13 M_{\odot}$ sequences ending up with $8.3 M_{\odot}$, can be expected to form neutron stars. Assuming angular momentum conservation during core collapse, their initial spin periods would be expected in the range $5 \dots 2 \text{ ms}$ (cf. Tab. 1), suitable for the scenario of magnetar driven superluminous supernovae (Metzger et al. 2015).

Assuming that the more massive Series B models would form black holes of at least $5 M_{\odot}$ (Obergaullinger & Aloy 2017), their average specific angular momentum would be $10^{16} \text{ cm}^2 \text{ s}^{-1}$ or more, implying they would be progenitor candidates for LGRBs within the collapsar scenario (Woosley 1993) (see Sect. 4 for a detailed discussion).

3.4. Mass loss history

As the adopted metallicity of our models is very small, radiation driven stellar winds are expected to be weak, and we do not discuss them here. Instead, as shown in Fig. 8, the mass loss rates of our models can become large in the contraction phases following core H and core helium burning. The reason is that the spin-up of the surface layers which accompanies the contraction would lead to over-critical rotation if the mass loss would not be enhanced. In this situation, even though the mass loss rate is formally computed by Eq. 2, and by MESA’s implicit mass loss routine in the case of near-critical rotation, it is not affected by the stellar wind mass loss rate, but rather determined by the amount of angular momentum which is required to be lost from the star for avoiding over-critical rotation (Langer 1998). As such, the mass loss rate is an inherent prediction of our model calculations. Whether or not the mass lost in this way can be transported to infinity, and if so which force could do this, depends on the achieved mass loss rate and will be discussed below. In our models, we argue that once mass is lost from the star it will not fall back, since the star is already very close to critical rotation.

Focusing on the mass loss rate increase after core helium exhaustion, we find it to be driven by two mechanisms. Most important, the models which undergo an overall contraction at this stage spin up, which leads them quickly to approach critical rotation. Strong mass loss is then required to avoid over-critical rotation. However, as shown in Fig. 8, also the lower mass models of Series A, which expand after core he-

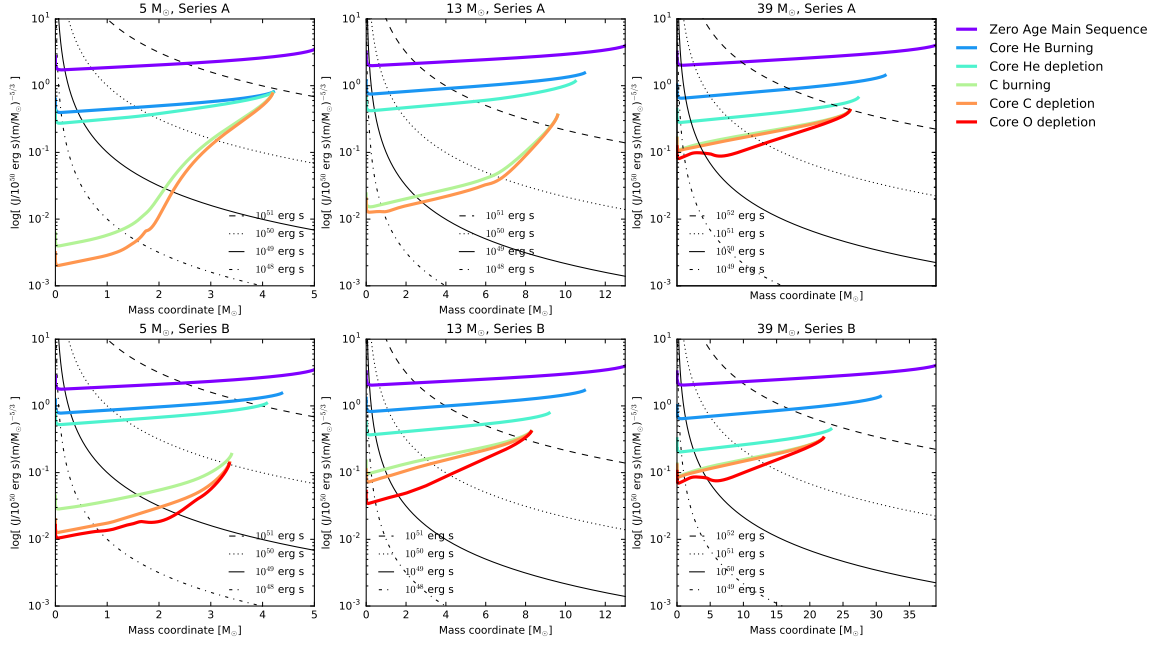


Figure 6. Integrated angular momentum $J(m)$ divided by $m^{5/3}$ as a function of the model’s mass coordinate, at main sequence (purple), start of core He burning (dark blue), core He depletion (light blue), during C burning (green), at C core depletion (orange) and at core O depletion (red), for Series A evolutionary sequences. Contours (labeled individually for each panel) represent lines of constant J .

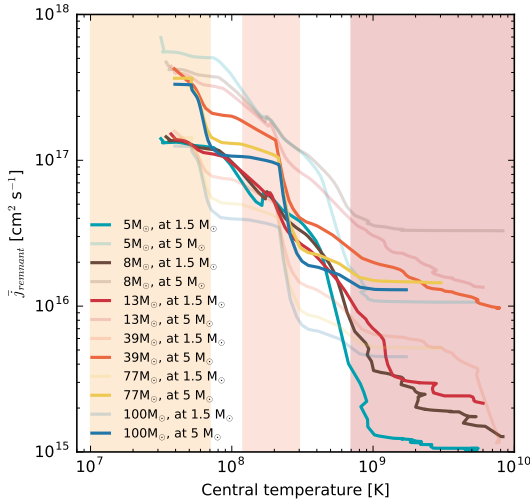


Figure 7. Average specific angular momentum of the innermost $1.5 M_{\odot}$ for models with $M < 20 M_{\odot}$, and of the innermost $5 M_{\odot}$ for models with $M \geq 20 M_{\odot}$ of our Series B models, as a function of central temperature in solid lines. The average specific angular momentum of the innermost $5 M_{\odot}$ for models with $M < 20 M_{\odot}$, and of the innermost $1.5 M_{\odot}$ for models with $M \geq 20 M_{\odot}$ are shown in transparent lines, for comparison.

lium exhaustion, show a partly significant increase in the mass loss rate. This is driven by the angular momentum transport in the lower mass models (cf., Sect. 3.3), which can be more significant than the spin-down effect due to the envelope expansion.

The overall post core-helium exhaustion mass loss of our model sequences (see Tabs. 1 and 2) is of the order of one solar mass, except for the $5 M_{\odot}$ and the $8 M_{\odot}$ models of Series A. Whereas the achieved mass loss rates in the more massive models are typically larger, their post-core helium burning life times are smaller. Also, in the lower mass models of Series B, both mass loss rate enhancement mechanisms work simultaneously, such that the corresponding $5 M_{\odot}$ model achieves the largest relative amount of mass being lost at this stage.

From the constant slope of the line for the contraction timescale in Fig. 5, it follows that the contraction accelerates according to a power law, and so does the mass loss. While the mass loss rates remain mostly around $10^{-3} M_{\odot} \text{yr}^{-1}$, they do approach $10^{-2} M_{\odot} \text{yr}^{-1}$ in the $39 M_{\odot}$ models.

It is uncertain whether the mass shed by our models during the later phases can be accelerated to large radii, since it is not due to radiatively accelerated winds, but dominated by the centrifugal force, which drops quickly with distance to the star. At the highest mass loss rates, assuming a wind velocity of only 500 km/s , the so-called photon-tiring limit (Heger & Langer 1996; Owocki & Gayley 1997; Grafener et al. 1998) is violated. I.e., such winds would violate energy conservation.

The momentum limit of radiation driven winds is met at much smaller mass loss rates. While in Wolf-Rayet stars, multiple scattering of photons allows this limit to be exceeded by a factor of a few (Springmann 1994), the winds may break down for much higher values. In Fig. 9 shows when in time the rate of the centrifugally driven mass loss exceeds the momentum limit by a factor of ten. We see that

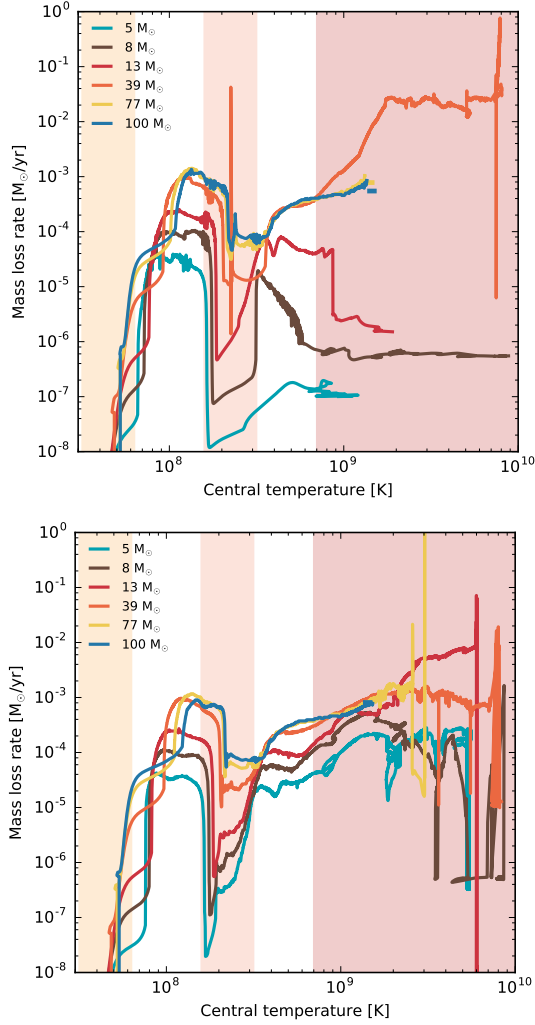


Figure 8. Mass loss rate as a function of central temperature for the evolutionary of Series A (top) and Series B (bottom). The temperature ranges with H, He and heavy element burning are highlighted.

in particular for the lower mass sequences, the concerns the bulk of the mass which is lost after core helium burning.

We conclude that mass lost by the stars after core helium exhaustion is likely to remain nearby the star. In addition, the outflows may be concentrated towards the equatorial plane of the star, which leads to higher local mass densities compared to the case of isotropic mass loss (van Marle et al. 2008). On the other hand, as the spin-up accelerates with time until the collapse of the iron core, and the mass loss rate increases with time correspondingly, any of the lost material is unlikely to be re-accreted by the star before the time of the SN. The chance to push the late mass loss to larger radii is largest for our highest mass models. However, as we shall argue below, their CSM at the time of their iron core collapse may be dominated by massive shells ejected in the course of their pulsational pair instability.

3.5. Magnetic fields

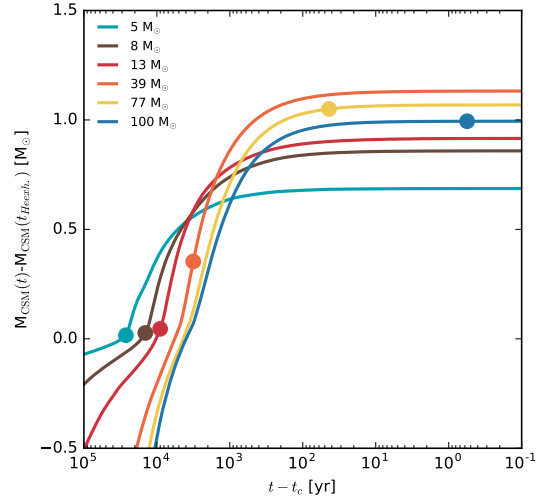


Figure 9. Time integrated mass loss rate with the end of core helium burning as zero point in time, as function of time, for six models of our Series B (bottom). Dots indicate where the mass loss rate becomes 10 times higher than that allowed by the momentum limit.

The rotation profile of our evolutionary sequences remains close to uniform during the main sequence due to the torques induced by dynamo-generated magnetic fields (Spruit 2002; Heger et al. 2005). This mechanism, as discussed in Sect. 3.3, is the main component transporting angular momentum in our evolutionary sequences. However, it also has the effect of generating strong magnetic fields in the stellar interior, especially in the late phases of stellar evolution.

Our pre-SN models, in particular, have strong magnetic fields, as illustrated in Fig. 10 for selected Series B models. As discussed in Sect. 3.1, chemical homogeneity is lost at the start of C burning. At this time the rotation profile becomes increasingly stratified, allowing for strong shear layers which promote the formation of strong magnetic fields. The fields in our pre-SN models in Fig. 10 are of the order of $10^{10} \dots 10^{11}$ G for the toroidal component and 10^8 G for the radial component near the interface between the iron core and the Si burning shell. This is considerably larger than the 5×10^9 G field found in the $15 M_{\odot}$ model of Heger et al. (2005). Assuming that the magnetic flux is preserved during core collapse, and that the produced neutron stars have $1.5 M_{\odot}$ and a radius of 15 km, leads to an enhancement of the B-field by a factor of 10^4 , i.e., to fields of order $10^{14} \dots 10^{15}$ G after the collapse. While flux freezing is certainly an oversimplification, according to Rembiasz et al. (2016), the MRI may enhance the B-field by up to a factor of 10 during the iron core collapse. Thus, while we can not reliably predict the post-collapse B-fields for our models, it appears plausible to assume that they do obtain magnetar strengths.

Our most massive models are evolved to the onset of the pair instability before oxygen ignition. At this stage, their toroidal core magnetic fields are of the order of $10^7 \dots 10^8$ G, which is comparable to the field values of our lower mass models at the same stage of evolution. According to Woosley

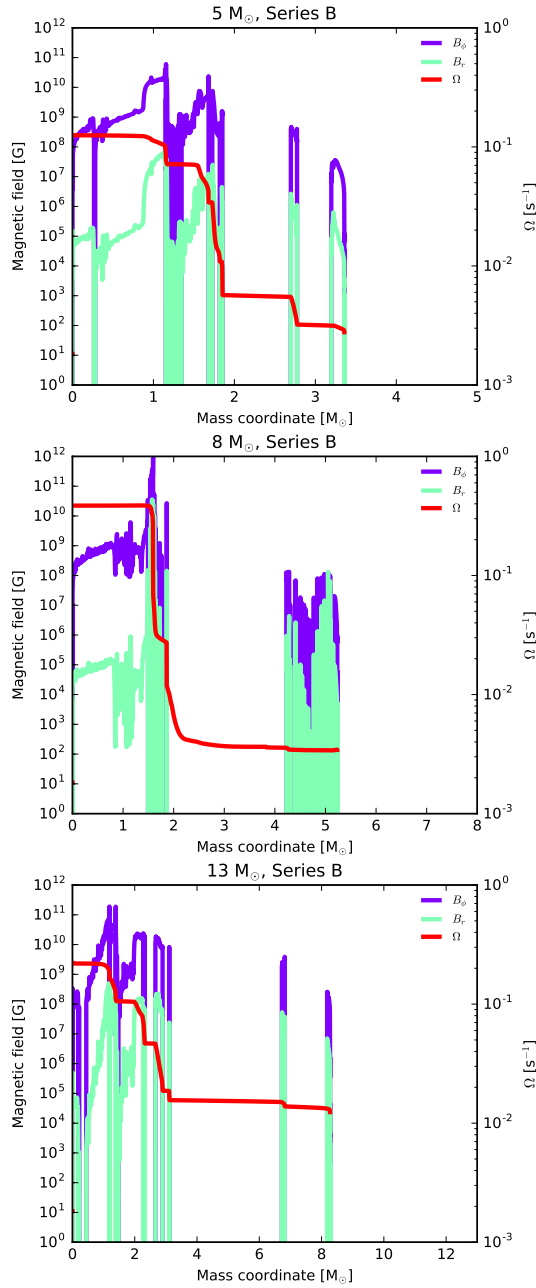


Figure 10. Polar and radial magnetic fields at the pre-SN stage for 3 different evolutionary sequences from Series B, along with their rotational frequency.

(2017), they can be expected to undergo a pulsational pair instability, which will ultimately end with the formation of an iron core, iron core collapse, and black hole formation. At the onset of the pair instability, the specific angular momentum of their cores exceeds $10^{16} \text{ cm}^2 \text{ s}^{-1}$. Assuming that the cores of these models do not suffer strong angular momentum loss during the pair-instability collapse and the further evolution towards iron core collapse would imply that magnetic fields would play a similar role in the final stages of these models as

they do for our lower mass models. However, the amount of core spin-down during the pulsational pair-instability process is yet unknown, and needs to be computed from corresponding models which include rotation.

The core specific angular momentum in our Series B models is an increasing function of mass, and therefore also the core magnetic field strength is expected to increase with mass. Our lowest mass models will form neutron stars, and the estimates above lead to magnetar strength B-fields. Since the transition mass between neutron star and black hole formation in the case of magneto-rotational collapse, and also the maximum neutron star mass in this case, is not well known (see [Obergaullinger & Aloy 2017](#)), our models contain the possibility that the largest masses which lead neutron stars reach a core specific angular momentum of $\sim 10^{16} \text{ cm}^2 \text{ s}^{-1}$ and could thus produce magnetar driven GRBs ([Metzger et al. 2015](#)). Above this transition mass, black holes and collapsar driven GRBs are expected, where magnetic fields would still be likely to strongly affect the accretion flow to the black hole and the formation of the GRB jet. As argued above, this may remain true even for our most massive models which undergo pulsational pair instability.

4. OBSERVABLE CONSEQUENCES

In the previous section we have seen that our Series B models show some general properties: They are all H-free and very helium-poor and thus qualify as progenitor models for Type Ic supernovae, they all develop rapidly rotating cores and generate strong magnetic fields before collapse, and they all suffer a rotationally induced mass loss of about $1 M_\odot$ briefly before they produce a supernova. Here, we will consider potential observational consequences of these properties during the supernova explosion. For this, we first discuss some general effects of the expected pre-SN CSM on the shock break-out and supernova light curve. After this, we discuss the more specific types of explosive events expected from our models as function of their mass.

4.1. Shock break-out

The first electromagnetic signals from SNe are released by the shock break-out, the moment when the shock reaches near the stellar surface and photons start to be released from the shock front (e.g., [Colgate 1974](#)). If an exploding star is surrounded by a dense CSM, the shock break-out signals can be strongly affected by it ([Ofek et al. 2010](#)).

The expected durations of the shock break-out from compact Wolf-Rayet progenitors are of the order of 1 sec. However, if they are surrounded by a dense CSM, photons released at the shock break-out are scattered in the dense CSM and the duration of the shock break-out can be extended to ~ 100 sec or more (e.g., [Balberg & Loeb 2011](#); [Svirski & Nakar 2014](#)).

A shock break-out from an exploding Wolf-Rayet star was observed in Type Ib SN 2008D and its duration was indeed about 400 sec ([Soderberg et al. 2008](#)). Although the progenitor has helium in this case, our progenitors contain dense enough CSM to have similar extended shock break-out sig-

Table 1. Initial and final parameters of the evolutionary sequences in Series B.

Initial mass [M_{\odot}]	5	8	13	39	77	100
Initial $\Omega/\Omega_{\text{crit}}$	0.89	0.84	0.79	0.69	0.67	0.67
CO core mass [M_{\odot}] ^a	4.08	6.13	9.18	23.17	41.75	52.47
Final mass [M_{\odot}]	3.36	5.23	8.27	22.05	40.68	51.47
$\Delta M_{\text{H}\rightarrow\text{He}}$ [M_{\odot}] ^b	0.36	0.55	1.04	4.58	13.58	20.41
$\Delta M_{\text{He}\rightarrow\text{final}}$ [M_{\odot}] ^c	0.68	0.86	0.92	1.13	1.07	0.99
f_M	0.27	0.19	0.12	0.06	0.20	0.62
Final Radius [cm]	2.15×10^{10}	2.27×10^{10}	1.52×10^{10}	2.72×10^{10}	3.31×10^{10}	4.14×10^{10}
Final T_{eff} [K]	1.63×10^5	1.72×10^5	1.16×10^5	2.68×10^5	3.63×10^5	2.96×10^5
Final H mass [M_{\odot}]	0	0	0	0	0	0
Final He mass [M_{\odot}]	0.04	0.05	0.03	0.06	0.03	0.04
Final Y_{surf}	0.10	0.08	0.07	0.03	0.02	0.02
Radius at $\tau = 1$ [cm]	2.78×10^{12}	1.98×10^{12}	3.32×10^{13}	2.16×10^{13}	1.67×10^{13}	1.33×10^{13}
$\bar{j}_{1.5M_{\odot}}$ [$\text{cm}^2 \text{s}^{-1}$]	1.03×10^{15}	1.27×10^{15}	2.16×10^{15}	1.15×10^{15}	5.15×10^{15}	4.50×10^{15}
$\bar{j}_{2M_{\odot}}$ [$\text{cm}^2 \text{s}^{-1}$]	1.38×10^{15}	1.92×10^{15}	3.17×10^{15}	2.38×10^{15}	6.35×10^{15}	5.76×10^{15}
$\bar{j}_{5M_{\odot}}$ [$\text{cm}^2 \text{s}^{-1}$]	–	3.25×10^{16}	1.28×10^{16}	9.36×10^{15}	1.29×10^{16}	1.16×10^{16}
P_{rot} ($1.5 M_{\odot}$ NS) [ms] ^d	4.66	3.76	2.22	4.15	0.93	1.06
E_{rot} ($1.5 M_{\odot}$ NS) [erg] ^d	2.07×10^{51}	3.18×10^{51}	9.11×10^{51}	2.60×10^{51}	5.18×10^{52}	3.96×10^{52}
Final fate	CCSN	CCSN	CCSN	CCSN	PPISN	PPISN

^a At core He depletion

^b Mass lost from between H and He burning, defined as $\Delta M_{\text{H}\rightarrow\text{He}} = \int_{T_{8c}>0.5}^{T_{8c}<1.2} \dot{M} dt$

^c Mass lost from He core depletion to the end of the simulation

^d Assuming the remnant is a $1.5 M_{\odot}$ neutron star, with 15 km radius, and with a moment of inertia of 2.27×10^{45} g cm^2 , computed using Eq. 19 from [Worley et al. \(2008\)](#)

nals to those found in SN 2008D. However, the dense CSM is constrained to exist only within about 10^{15} cm in the case of SN 2008D ([Soderberg et al. 2008](#)) and the dense CSM needs to exist only near the progenitor (see [Moriya et al. 2015](#) for a different idea). In addition, we note that this simple picture is based on a spherically symmetric model.

For our models, the CSM at the time of the SN is expected to be very aspherical. If we assume that in the polar direction, along the rotation axis of the star, ordinary radiation driven wind mass loss has dominated, shock break-out could occur along this direction on the timescales mentioned above.

On the other hand, as argued in Sect. 3.4, the bulk of the centrifugally expelled mass shortly before the supernova explosion might remain in a disk-like configuration embedding the star. In this case, the SN shock may remain embedded for some time, and the early light curve of the SN could be strongly affected by the SN-CSM interaction.

4.2. CSM interaction

When the SN ejecta collides with a dense CSM, the collision efficiently converts the ejecta kinetic energy to radiation. This extra radiation alters both, light curve and spectral properties of SNe (e.g. [Sorokina et al. 2016](#)). An estimate of the radiation energy produced by the interaction is obtained by assuming an inelastic collision of the ejecta with mass M_{ej}

and velocity v_{ej} with a shell with a mass of M_{sh} and velocity v_{sh} . Momentum conservation results in a fraction of kinetic energy that is removed from the ejecta as

$$\Delta E = E_{\text{kin,ej}} f_M f_v^2 \quad (5)$$

where $E_{\text{kin,ej}} = M_{\text{ej}} v_{\text{ej}}^2 / 2$ is the kinetic energy of the supernova, and

$$f_M = \frac{M_{\text{sh}}}{M_{\text{ej}} + M_{\text{sh}}}, \quad (6)$$

and

$$f_v = \frac{v_{\text{ej}} - v_{\text{sh}}}{v_{\text{ej}}} \quad (7)$$

account for the relative mass and velocity difference between shell and ejecta.

Whereas the shell velocity v_{sh} is likely small for our models, such that $f_v \simeq 1$ (except for the highest masses; see below), we need to estimate the SN ejecta mass for our models to evaluate the mass ratio f_M . Corresponding model calculations do not yet go far enough in time to give well-founded theoretical ejecta masses for magneto-rotational supernovae ([Obergaullinger & Aloy 2017](#)). However, ejecta mass estimates for observed SN Ic-bl are in part quite large (e.g., [Mazzali et al. 2017](#)). We therefore assume here that except for a neutron star of $1.5 M_{\odot}$ or, for higher masses, a black hole

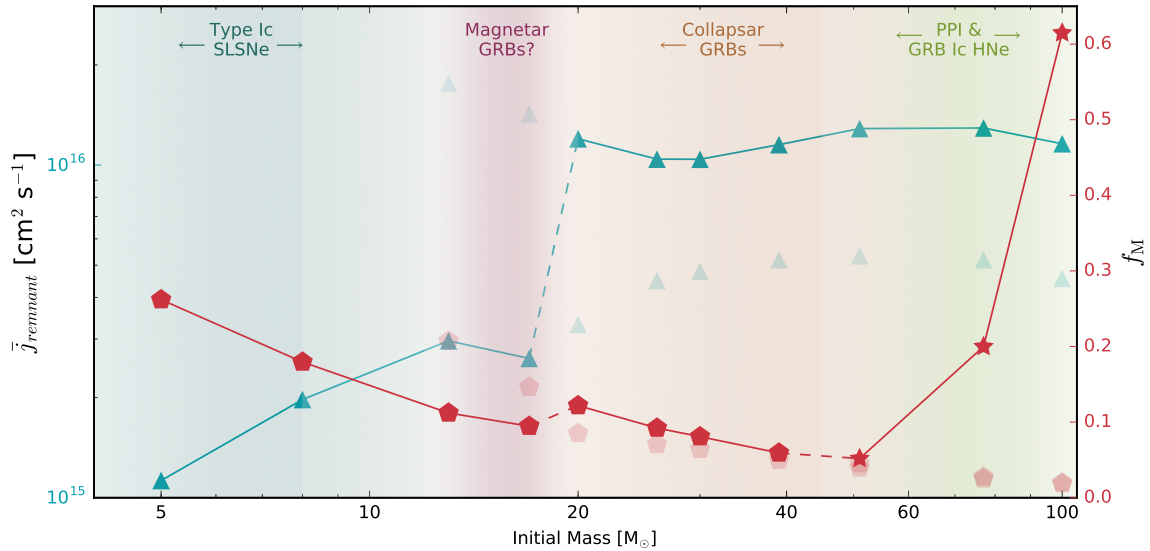


Figure 11. Average angular momentum at core O depletion of the first $1.5 M_{\odot}$, for models with mass $M < 20 M_{\odot}$, and first $5 M_{\odot}$ for the rest (left axis, blue triangles); and the ratio between shell and ejecta masses for the same remnant masses (right axis, red pentagons), as a function of initial mass for Series B models. The values for converse masses are added in lower saturation for comparison. The ratio between shell and ejecta mass for models that undergo pulsational pair instability is also calculated (red stars), with ejected shell masses according to Woosley (2017).

of $5 M_{\odot}$, the remainder of the star will be expelled in the SN. Fig. 11 shows that with this assumption, the mass ratio f_M drops from near 0.3 for our $5 M_{\odot}$ sequence to 0.06 at $39 M_{\odot}$, indicating a corresponding drop in the maximum possible fraction of SN kinetic energy to be converted into light through SN-CSM interaction. The steep rise of f_M for our highest masses in Fig. 11 assumes massive shells ejected due to the pulsational-pair instability, and will be discussed in Sect. 4.4.

4.3. Lowest masses: magnetar powered Type Ic SLSNe

In a recent analysis of 38 H-poor SLSNe in the scope of the magnetar model, Nicholl et al. (2017b) derive the main parameters of such explosions in terms of initial magnetar spin period (1.2...4 ms) and B-field ($0.2 \times 10^{14} \dots 1.8 \times 10^{14}$ G), ejecta mass ($2.2 \dots 12.9 M_{\odot}$), and kinetic energy ($1.9 \times 10^{51} \dots 9.8 \times 10^{51}$ erg). Notably, the magnetar spin and ejecta masses are in nice agreement with our lower mass models. While our estimates for the initial B-fields of the neutron stars are not reliable, we argued in Sect. 3.5 that they might well be of magnetar strength. Our lower mass models, may thus be suitable to provide Type I SLSNe within the magnetar model (e.g., Woosley 2010; Kasen & Bildsten 2010).

We can estimate the initial rotational energy of a neutron star forming from our $5 M_{\odot}$, $8 M_{\odot}$, and $13 M_{\odot}$ Series B models as 2.1×10^{51} erg, 3.2×10^{51} erg, and 9.1×10^{51} erg (cf. Sect. 3.3). Assuming the average SLSNI kinetic energy of 4×10^{51} erg (see above), radiation with an energy of up to $\sim 10^{51}$ erg could in principle be liberated by the interaction of the SN ejecta with the rotationally driven pre-SN mass loss of about $1 M_{\odot}$ (Sect. 3.4). A larger than canonical SN kinetic

energy could indeed be plausible since magneto-rotational effects would be expected to be very significant here.

Compared to the rotational energy of a magnetar, the interaction luminosity is smaller but not negligible. To demonstrate this, we have computed a hypothetical luminosity that can be released from CSM interaction in our models, assuming the lost matter has continuously been shed in a spherically symmetric configuration, and with a small constant velocity ($v_w = 0.2 \text{ km s}^{-1}$), with a density profile given by $\rho(r) = \dot{M}/(4\pi r^2 v_w)$. Adopting the simple inelastic collision model (Eq. 7), we estimate the liberated interaction luminosity as a function of time for our lowest mass models by calculating the change in kinetic energy as the ejecta decelerates due to the interaction (Fig. 12). We take into account the change in kinetic energy at each time step and assume that all the released kinetic energy is converted to radiation. This method conserves the momentum of the ejecta and takes into account the change in kinetic energy as it grows in mass. We compare this with the Type I SN 2015bn, arguing that the luminosity produced by the interaction should be significant even if the main source of luminosity is the central engine.

Our estimate of the produced amount of light from the CS interaction does not assume a complete thermalisation of the SN kinetic energy, but accounts for the constraints imposed by momentum conservation. Whereas it provides an upper limit, since even this reduced amount of kinetic energy will not be all transformed into light, Moriya et al. (2013) showed that it is expected to match the true efficiency within an order of magnitude. Furthermore, since the CSM mass distribution of our models is not well known, and likely aspherical, Fig. 12 should not be taken as a light curve prediction from our models, but only as an illustration of the potential effects

which the interaction may have on the SN light curve. Hydrodynamical effects and the diffusion of radiation through the dense CSM will shape the actual light curve, but a detailed light curve calculation is beyond the scope of this paper.

It was recently suggested that some external energy source, most likely from CSM interaction, may be required to explain various features of SLSNe Ic. Many of them show prominent bumps in the declining phase of their light curves (In-serra et al. 2017), and Fig. 12 shows that the pre-SN mass loss from our models may be a candidate to explain those. Furthermore, Chen et al. (2017b) find evidence for additional energy input in the period of 2 d before until 22 d after maximum light from the spectral evolution of the Type Ic SLSN LSQ14mo, which they tentatively advocate to circumstellar interaction.

The 3D distribution of the mass around the progenitor, with mass likely concentrated towards the equatorial plane, and the temporal behavior of the mass loss in our models may play a role in shaping the SN observables. Short episodes of intense mass loss, such as in our $8 M_{\odot}$ evolutionary sequence, may lead to dense mass shells, which could give rise to significant ups and downs in the light curve. Moriya & Maeda (2012) pointed out that detached shells necessarily give rise to prominent “dips” in the light curve, which is often observed in SLSNe Ic (Nicholl & Smartt 2016).

We conclude that while the major brightness of magnetar driven Type Ic SLSNe is expected to be provided through heating from the magnetar spin-down (Kasen & Bildsten 2010; Woosley 2010), significant deviations from the simple magnetar powered light curves are expected due to the interaction between ejecta and the CSM, based on our pre-SN models.

4.4. Intermediate masses: magnetar-driven Type Ic GRB SNe?

From the properties of our models, we are not able to draw the mass limit between neutron star and black hole formation. Even for non-rotating massive stars, this mass limit is not yet well known, since multi-dimensional effects are essential in core collapse supernovae (e.g., Janka et al. 2016). Parametrised 1D core collapse simulations even suggest some stochasticity in the outcome of core collapse within a certain mass range, rather than a clearcut mass limit (e.g., Sukhbold et al. 2016). Whether the situation is similar in the case of a magneto-rotational core collapse is unclear. However, black hole formation above a certain mass threshold is expected also in this case (Obergaullinger & Aloy 2017). This provides the major feature dividing explosions which are magnetar powered from those which are powered by black hole accretion. Therefore, keeping in mind that the situation may be more complex, we remain at discussing certain mass ranges for certain outcomes.

In this spirit, it may also be possible that magnetar driven GRBs and associated hypernovae are produced near the BH/NS mass limit. In fact, within the scenario of Thompson & Duncan (1993) for B-field production during core collapse, the highest B-fields would be expected for the fastest rotat-

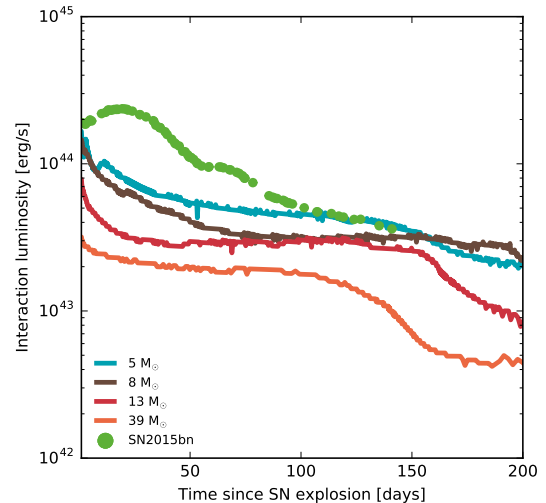


Figure 12. Interaction luminosity adopting a typical SLSNI kinetic energy of 4×10^{51} erg, calculated using Eq.5, and assuming the CSM material has spread with a small velocity of $v_w = 0.2$ km/s (see text), for four Series B models with the indicated initial masses. The observed light curve of SN2015bn (from Nicholl et al. (2016)) was included for reference, and is displayed with a 10 day shift with respect to its maximum luminosity.

ing neutron stars, which we find near the BH/NS mass limit. There, the neutron star masses may also be largest, which may lead to the most rapidly rotating neutron stars. (Metzger et al. 2015) argue that for sufficiently strong B-fields, a pulsar rotation period near 2 ms may lead to a magnetar driven GRB. Tab. 1) and Fig. 11 show that this may be within reach for our progenitor models with initial masses below but near $20 M_{\odot}$. This scenario is attractive because it can possibly account for ultra-long GRBs as the one reported by Greiner et al. (2015).

4.5. High masses: collapsar driven Type Ic GRB SNe

As discussed above, we can expect black holes rather than neutron stars being formed above a certain mass limit, even when rotation and magnetic fields are strongly affecting the iron core collapse (Obergaullinger & Aloy 2017). Since the black holes are significantly more massive than neutron stars, and as the specific angular momentum in our models generally increases outwards, their average specific angular momentum will be larger than that of the neutron stars in the lower mass models. This effect is augmented by a significant drain of core angular momentum in the lower mass stars due to their relatively large lifetime after core helium exhaustion (Sect. 3.3). As seen in Fig. 11, when we assume a black hole mass of $5 M_{\odot}$, their specific angular momenta exceed $10^{16} \text{ cm}^2 \text{ s}^{-1}$, and the models are thus thought to be suitable progenitor models for IGRBs (Yoon & Langer 2005; Woosley & Heger 2006; Yoon et al. 2006).

I GRBs are associated with hyperenergetic Type Ic SNe. Our more massive models have larger ejecta masses, and are expected to convert only up to about 5% of the SN kinetic energy into radiation through CSM interaction. These supernovae have kinetic energies of the order of 10^{52} erg, but they are not superluminous, and only few of them have been observed in significant detail until today (see, for example, [Cano et al. 2017](#)).

At face value, our estimate would imply that up to 5×10^{50} erg of radiation could be produced through CSM interaction in GRB SNe. However, we have strong evidence that these hypernova explosions are strongly aspherical (e.g., [Maeda et al. 2002](#)), with much higher ejecta velocities in polar than in equatorial direction. At the same time, it is likely that the pre-supernova mass loss of our model stars would be emitted predominantly into directions of low latitude. The hypernova might thus catapult its fastest ejecta into the polar holes of the CSM distribution. The true interaction luminosity could therefore be far below the number quoted above. Still, around $1 M_{\odot}$ of material is expected to sit close to the exploding star and, depending on the viewing angle, it may show up in absorption or emission.

Also the GRB jet is expected to be launched in the polar direction. As the densest CSM is likely located in the equatorial plane, an interaction between the jet and the CSM may not occur often. However, several low-luminosity IGRBs like GRB060218/SN 2006aj (e.g., [Campana et al. 2006](#); [Mazzali et al. 2006](#); [Pian et al. 2006](#); [Soderberg et al. 2008](#)) are suggested to occur in a dense CSM surrounding the progenitor stars (e.g., [Irwin & Chevalier 2016](#)).

4.6. *Very high masses: interaction powered Type Ic superluminous supernovae*

At the highest masses considered here, above $50 M_{\odot}$, the centrifugally supported ejection of about $1 M_{\odot}$ of material is perhaps unimportant. However, the oxygen cores of the considered models become e^{\pm} -pair-unstable before oxygen ignition, and may undergo pair instability pulses ([Woosley et al. 2007](#); [Chatzopoulos & Wheeler 2012b](#); [Woosley 2017](#); [Yoshida et al. 2016](#)). In non-rotating models, [Woosley \(2017\)](#) has shown these pulses may eject shells with masses up to $28 M_{\odot}$, with higher mass shells for more massive stars. Notably, the models which produce the so called pulsational pair-instability SNe will eventually undergo iron core collapse. Assuming that during the pair-induced pulsations the core angular momentum remains unchanged, this core collapse may produce a IGRB, or at least an engine-driven hypernova. It may therefore be a common outcome from our most massive models to produce an interaction powered SLSN of Type Ic, where the interaction occurs between a massive Type Ic hypernova and a massive circumstellar shell consisting predominantly of carbon and oxygen. However, we note that the effect of the pulsations on the core angular momentum distribution remains yet to be determined by detailed models.

Within this scenario, depending on the uncertain mass of the black hole produced in the collapse, the conversion effi-

ciency of supernova kinetic energy to light may be very high (Fig. 11). With the central engine producing a hypernova, the kinetic energy of the ejecta would also be very high. As the ejecting force which lifts off the massive shell during a pair-induced pulse is rooted deep inside the star, where ratio of centrifugal force to gravity is well below one, the circumstellar shell produced in this event is expected to be far less aspherical than the wind-produced shells discussed above. Therefore, even though the high velocity of the shell produced by the pair pulsation may lead to f_v -values below one (cf., Eq. 7), this scenario may potentially produce the brightest interaction driven supernovae, with a total energy content of the radiation of the order of 10^{52} erg, competing with the brightest possible magnetar driven supernova ([Sukhbold & Woosley 2016](#)).

PPI supernovae may in principle also produce interaction dominated Type Ic supernovae if they would not rotate. However, according to the current core collapse supernova models ([Heger & Woosley 2002](#), [Takahashi et al. 2016](#)), the final collapse of the core into a black hole in non-rotating stars of such high mass may actually not produce a core collapse supernova at all.

It may be interesting to compare our model predictions with the SLSN Ic Gaia2016apd. This supernova is peculiar as it shows an extremely blue continuum, much more so than any other of the generally already very blue Ic SLSNe ([Yan et al. 2017](#)). [Nicholl et al. \(2017a\)](#) explain this as a magnetar powered supernova with rather ordinary magnetar parameters ($P = 1.9$ ms, and $B = 2 \cdot 10^{14}$ G) but with a very strong central engine, giving rise to a SN kinetic energy of at least 3×10^{51} erg, possibly $> 10^{52}$ erg. [Tolstov et al. \(2017\)](#), however, by employing multi-group radiative transfer calculations, do not succeed to explain the extremely blue continuum with this scenario. They find a hypernova interacting with a fast and massive CO-shell as most likely explanation for SN Gaia2016apd. We note that this at first glance very exotic scenario is a natural prediction from our most massive progenitor models.

At even higher masses than considered in our work, we would expect plain pair instability supernovae ([Heger & Woosley 2002](#); [Kozyreva et al. 2014, 2017](#); [Kasen et al. 2011](#); [Dessart et al. 2013](#)). Whereas the influence of rotation on PISNe has been investigated ([Glatzel et al. 1985](#); [Chatzopoulos & Wheeler 2012a,b](#); [Chatzopoulos et al. 2013](#)), the magneto-rotational PI-collapse remains yet to be studied.

5. DISCUSSION

The results derived above have been obtained through stellar evolution calculations in the frame of the CHE scenario ([Yoon & Langer 2005](#); [Woosley & Heger 2006](#)), in which we artificially increased the diffusion coefficient for rotationally induced mixing. For this diffusion coefficient, and its dependence on the stellar rotation rate, only local and linear approximations are known (cf., [Heger et al. 2000](#); [Spruit 2002](#)), while the non-linear behavior, which might be particularly relevant in the case of extreme rotation considered here, is not known from first principles.

While used ad-hoc, some retrospect support for the enhancement of the mixing coefficient may be drawn from the fact that the corresponding models do reproduce Type Ic supernova progenitors, which has proven notoriously difficult for CHE models using the nominal diffusion coefficient, in particular in the lower mass range of the models considered here (Yoon et al. 2006). We emphasise that this does not alleviate the need to find confirmation for the faster mixing, through multidimensional MHD calculations as well as through observations.

In any case, our calculations produce rapidly rotating nearly bare CO cores at the end of core He burning, and the observations of GRB supernovae and Type Ic SLSNe tell us that such objects may indeed be required to explain what we see. While binary evolutionary channels have been proposed to produce such objects (e.g., Detmers et al. 2008; Podsiadlowski et al. 2010; Fryer et al. 2014; Marchant et al. 2016), we point out that once they are formed, their further evolution will be rather independent of the the formation channel. The reason is that the chemical structure is uniquely defined — they are just CO stars —, and at least in the framework of the Spruit-Taylor dynamo the angular momentum distribution will also be homogeneous, as at this stage there are no entropy barriers inside the stars.

We therefore suggest that whether CHE is the dominant production channel or not, and independent of whether the mixing coefficient is really as large as we assumed, our evolutionary models do describe the post-core He burning evolution of the progenitors of GRB supernovae and Type Ic SLSNe. I.e., the overall contraction and spin-up induced mass loss, as well as the mass dependence of the specific angular momentum of the compact remnant (Fig. 11), are not expected to depend significantly on the formation history of the rapidly rotating CO stars.

When considering the spin-up induced mass loss a generic prediction of the magnetar and collapsar models discussed here, the diagnostics of vigorous pre-SN mass loss and circumstellar shells in the observations of related supernovae becomes crucial, in the sense that a failure to find evidence of such mass loss may question the underlying model. However, as discussed in Sect. 4, even though such diagnostics are often difficult to obtain, many indications for significant CSM interaction have already been found, at least in SLSNe.

At the same time, the detection of large amounts of CSM close to the exploding star in a Type Ic supernova would not prove the spin-up scenario. Other ways of achieving this have been proposed, e.g., through non-conservative close binary mass transfer after core-He exhaustion (Chevalier 2012), through the transport of energy by gravity waves excited in the deep interior during the late burning stars from the core to the stellar surface (Fuller & Ro 2017), or through violent pulsations (Heger et al. 1997; Yoon & Cantiello 2010; Moriya & Langer 2015). In contrast to these mechanisms, the one discussed here works only in extremely rapidly rotating stars and thus in rotation powered supernovae. In that sense, the indications for CSM interaction in a large number of Type I SLSNe is supporting the scenario of a rapidly rotating pro-

genitor, independent of the need for this within the magnetar scenario.

In this work, we have computed only models with an extremely small metallicity ($Z_{\odot}/50$). While massive stars with such low metallicities exist in the local universe (Izotov & Thuan 2016), and Type I SLSNe (Chen et al. 2017a; Schulze et al. 2018) and IGRBs (Graham & Fruchter 2017) do preferentially occur at sub-solar metallicity, the observationally deduced metallicities are generally larger than $Z_{\odot}/50$.

We have chosen such a low metallicity, since from the calculations of Yoon et al. (2006) and Marchant et al. (2016) which explored CHE at various metallicities, it was clear that this would open the maximum mass range for this scenario, and — as discussed above — once a rapidly rotating CO star is produced, its progenitor evolution does not affect its final evolution. Indeed, as ordinary stellar winds are too weak to affect the post-core helium burning evolution, the evolution through the late burning stages will also be largely metallicity-independent.

However, within the CHE production channel of Type I SLSNe and IGRBs, metallicity will foreseeably strongly affect the formation rates of these events, mediated through the metallicity dependence of radiation driven winds (Mokiem et al. 2007; Crowther 2006). In fact, to the extent that even in metal-rich stellar surfaces, iron is the main element driving the wind (Vink & de Koter 2005), the metallicity dependence of the final core angular momentum in CHE models computed with enhanced mixing coefficients is expected to be very similar for the highest masses to that obtained by Yoon et al. (2006). This is confirmed by comparing the numbers in Tabs. 1 and 2 with those obtained by Yoon et al. (2006) for their lowest considered metallicity ($Z=0.00001$). Therefore, the main effect of metallicity in our models is expected to be that higher metallicity lowers the mass threshold above which the CHE scenario can not work any more due to wind induced spin-down during H- and He-burning (see also Marchant et al. 2016). Grids of detailed models are required to confirm this, and to compare with the empirical magnetar spin-metallicity correlation suggested by Chen et al. (2017a) although the correlation might not be as strong as originally suggested (e.g., Nicholl et al. 2017b; De Cia et al. 2017).

One might expect from our models that the low metallicity bias of SLSNe I may be smaller than that of IGRBs, since originating from a lower mass range implies that wind spin down is less important. Currently, observations seem to imply the opposite trend (Graham & Fruchter 2017; Chen et al. 2017a). However, Yoon et al. (2006) found that the lower mass limit for chemically homogeneous evolution increases with metallicity, which could strengthen the low metallicity bias for SLSNe I. Model grids with varying metallicity are urgently needed to enlighten this point.

In the same spirit, one might consider the frequency of the the various types of explosions expected from our models in connection with the predicted corresponding mass ranges, assuming an initial mass function. However, as the numbers might change considerably when also a convolution with the respective metallicity trends would be included, we refrain

from such an attempt here, but point out that future model grids with varying metallicity would allow to do this. The only statement we may make in this direction is that the outcome expected for the most massive stars considered here, the superluminous interacting Ic hypernova, is perhaps indeed the observationally rarest case (as pointed out by our referee).

6. CONCLUSIONS

We obtain fast spinning, almost pure CO stars at core helium exhaustion, with high angular momenta, corresponding to progenitors of SLSNe, Type Ic SNe and GRBs, computed through evolutionary sequences for rapidly rotating low metallicity massive stars that evolve quasi-chemically homogeneously. Our models using the nominal rotational mixing efficiency correspond well to earlier such calculations (Yoon & Langer 2005; Woosley & Heger 2006; Yoon et al. 2006; Szécsi et al. 2015). When invoking enhanced rotational mixing, we obtain rapidly rotating CO stars. We argue that these represent the progenitors of Type Ic SLSNe and IGRBs, independent of the evolutionary scenario through which these explosions are actually produced, in as much as rapid rotation and the absence of helium are observational requirements.

We follow the evolution of these objects through the late burning stages until the pre-collapse state. We find that due to the lack of a helium envelope, they contract and do so at an accelerated rate, following the neutrino-mediated Kelvin-Helmholtz timescale (Eq. 4). The corresponding spin-up leads to centrifugal shedding of significant amounts of mass during the last hundreds of years of the stars evolution, which will affect the display of the ensuing supernova explosion. We further find a trend of increasing specific angular momentum in the innermost cores with mass. Together with the fact that our mass range covers the NS/BH as well as the BH/pair-instability transition, this leads to the suggestion of the following explosion types as function of mass.

For the lowest considered masses, with ejecta masses in the range $2M_{\odot} \dots 20M_{\odot}$, our models predict NS spin rates as required for magnetar-powered Type Ic SLSNe (Metzger et al. 2015), and with magnetic fields that are consistent with those

derived to reproduce the light curves of SLSNe Nicholl et al. (2017b). In addition to the magnetar-heating in such events, our models show that in addition, up 20% of the SN kinetic energy could be converted into radiation through CSM interaction. Near the BH formation mass limit, magnetar-driven (ultra-)long GRBs may also be possible.

Above the BH formation threshold, the average specific angular momentum of the compact object reaches $\sim 10^{16} \text{ cm}^2 \text{ s}^{-1}$, and IGRBs are expected within the collapsar scenario (Woosley 1993), accompanied by Type Ic hypernovae (i.e., supernovae with a large kinetic energy). The predicted mass of the close range CSM amounts here to a few percent of the mass of the hypernova ejecta, with an efficient thermalisation potentially prevented by geometry effects.

The oxygen cores of the largest mass stars considered here become e^{\pm} -pair unstable (the last stage considered by our models), and are expected to eject massive shells due the pulsational pair instability (Woosley 2017). As for the lower mass cases, the central engine is expected to produce a hypernova, which here would collide with the massive CO-shells ejected earlier to produce an interaction dominated Type Ic SLSN with up to 10^{52} erg of energy in the form of light.

The properties of the explosion phenomena discussed above are anticipated based upon our current knowledge. Therefore, besides exploring the pre-supernova model parameter space in greater depth, multi-D models of the pre-SN CSM evolution, and of the magneto-rotational collapse phase would be valuable next steps. This would allow for consistent calculations of the resulting light curves and spectra of the supernova phase, which are ultimately needed as a test of the models presented here.

Acknowledgments. We would like to acknowledge valuable discussions with Sergei Blinnikov, Pablo Marchant, Thomas Tauris and Alexey Tolstov, and very useful comments from the anonymous referee of our paper. We would like to thank Matt Nicholl for providing the data for SN2015bn.

Software: MESA (v10000; Paxton et al. (2011, 2013, 2015, 2017))

REFERENCES

- Balberg, S., & Loeb, A. 2011, *MNRAS*, 414, 1715
- Bjorkman, J. E., & Cassinelli, J. P. 1993, *ApJ*, 409, 429
- Böhm-Vitense, E. 1958, *ZA*, 46, 108
- Brott, I., de Mink, S. E., Cantiello, M., et al. 2011, *A&A*, 530, A115
- Campana, S., Mangano, V., Blustin, A. J., et al. 2006, *Nature*, 442, 1008
- Cano, Z., Wang, S.-Q., Dai, Z.-G., & Wu, X.-F. 2017, *Advances in Astronomy*, 2017, 8929054
- Chatzopoulos, E., & Wheeler, J. C. 2012a, *ApJ*, 748, 42
- . 2012b, *ApJ*, 760, 154
- Chatzopoulos, E., Wheeler, J. C., & Couch, S. M. 2013, *ApJ*, 776, 129
- Chen, T.-W., Smartt, S. J., Yates, R. M., et al. 2017a, *MNRAS*, 470, 3566
- Chen, T.-W., Nicholl, M., Smartt, S. J., et al. 2017b, *A&A*, 602, A9
- Chevalier, R. A. 2012, *ApJL*, 752, L2
- Colgate, S. A. 1974, *ApJ*, 187, 333
- Crowther, P. A. 2006, ArXiv Astrophysics e-prints, astro-ph/0606580
- De Cia, A., Gal-Yam, A., Rubin, A., et al. 2017, ArXiv e-prints, arXiv:1708.01623 [astro-ph.HE]

- Della Valle, M., Chincarini, G., Panagia, N., et al. 2006, *Nature*, 444, 1050
- Dessart, L., Waldman, R., Livne, E., Hillier, D. J., & Blondin, S. 2013, *MNRAS*, 428, 3227
- Detmers, R. G., Langer, N., Podsiadlowski, P., & Izzard, R. G. 2008, *A&A*, 484, 831
- Drake, A. J., Djorgovski, S. G., Mahabal, A., et al. 2009, *ApJ*, 696, 870
- Ekström, S., Meynet, G., Maeder, A., & Barblan, F. 2008, *A&A*, 478, 467
- Ekström, S., Georgy, C., Eggenberger, P., et al. 2012, *A&A*, 537, A146
- Flaugher, B., Diehl, H. T., Honscheid, K., et al. 2015, *AJ*, 150, 150
- Friend, D. B., & Abbott, D. C. 1986, *ApJ*, 311, 701
- Fryer, C. L., Rueda, J. A., & Ruffini, R. 2014, *ApJL*, 793, L36
- Fuller, J., & Ro, S. 2017, ArXiv e-prints, [arXiv:1710.04251](https://arxiv.org/abs/1710.04251) [astro-ph.SR]
- Fynbo, J. P. U., Watson, D., Thöne, C. C., et al. 2006, *Nature*, 444, 1047
- Gal-Yam, A., Fox, D. B., Price, P. A., et al. 2006, *Nature*, 444, 1053
- Gehrels, N., Norris, J. P., Barthelmy, S. D., et al. 2006, *Nature*, 444, 1044
- Georgy, C., Ekström, S., Meynet, G., et al. 2012, *A&A*, 542, A29
- Georgy, C., Ekström, S., Eggenberger, P., et al. 2013, *A&A*, 558, A103
- Glatzel, W., Fricke, K. J., & El Eid, M. F. 1985, *A&A*, 149, 413
- Grafener, G., Hamann, W.-R., Hillier, D. J., & Koesterke, L. 1998, *A&A*, 329, 190
- Graham, J. F., & Fruchter, A. S. 2017, *ApJ*, 834, 170
- Greiner, J., Mazzali, P. A., Kann, D. A., et al. 2015, *Nature*, 523, 189
- Grevesse, N., Noels, A., & Sauval, A. J. 1996, in *Astronomical Society of the Pacific Conference Series*, Vol. 99, *Cosmic Abundances*, ed. S. S. Holt & G. Sonneborn, 117
- Hamann, W.-R., Koesterke, L., & Wessolowski, U. 1995, *A&A*, 299, 151
- Heger, A., Jeannin, L., Langer, N., & Baraffe, I. 1997, *A&A*, 327, 224
- Heger, A., & Langer, N. 1996, *A&A*, 315, 421
- Heger, A., Langer, N., & Woosley, S. E. 2000, *ApJ*, 528, 368
- Heger, A., & Woosley, S. E. 2002, *ApJ*, 567, 532
- Heger, A., Woosley, S. E., & Spruit, H. C. 2005, *ApJ*, 626, 350
- Inserra, C., Smartt, S. J., Jerkstrand, A., et al. 2013, *ApJ*, 770, 128
- Inserra, C., Nicholl, M., Chen, T.-W., et al. 2017, *MNRAS*, 468, 4642
- Irwin, C. M., & Chevalier, R. A. 2016, *MNRAS*, 460, 1680
- Izotov, Y. I., & Thuan, T. X. 2016, *MNRAS*, 457, 64
- Janka, H.-T., Melson, T., & Summa, A. 2016, *Annual Review of Nuclear and Particle Science*, 66, 341
- Kaiser, N., Burgett, W., Chambers, K., et al. 2010, in *Proc. SPIE*, Vol. 7733, *Ground-based and Airborne Telescopes III*, 77330E
- Kasen, D., & Bildsten, L. 2010, *ApJ*, 717, 245
- Kasen, D., Woosley, S. E., & Heger, A. 2011, *ApJ*, 734, 102
- Kozyreva, A., Blinnikov, S., Langer, N., & Yoon, S.-C. 2014, *A&A*, 565, A70
- Kozyreva, A., Gilmer, M., Hirschi, R., et al. 2017, *MNRAS*, 464, 2854
- Langer, N. 1989, *A&A*, 210, 93
- . 1991, *A&A*, 252, 669
- . 1998, *A&A*, 329, 551
- Maeda, K., Nakamura, T., Nomoto, K., et al. 2002, *ApJ*, 565, 405
- Marchant, P., Langer, N., Podsiadlowski, P., Tauris, T. M., & Moriya, T. J. 2016, *A&A*, 588, A50
- Margalit, B., Metzger, B. D., Thompson, T. A., Nicholl, M., & Sukhbold, T. 2018, *MNRAS*, 475, 2659
- Mazzali, P. A., Sauer, D. N., Pian, E., et al. 2017, *MNRAS*, 469, 2498
- Mazzali, P. A., Deng, J., Nomoto, K., et al. 2006, *Nature*, 442, 1018
- Metzger, B. D., Margalit, B., Kasen, D., & Quataert, E. 2015, *MNRAS*, 454, 3311
- Modjaz, M., Liu, Y. Q., Bianco, F. B., & Graur, O. 2016, *ApJ*, 832, 108
- Mokiem, M. R., de Koter, A., Vink, J. S., et al. 2007, *A&A*, 473, 603
- Moriya, T. J., Blinnikov, S. I., Tominaga, N., et al. 2013, *MNRAS*, 428, 1020
- Moriya, T. J., & Langer, N. 2015, *A&A*, 573, A18
- Moriya, T. J., & Maeda, K. 2012, *ApJL*, 756, L22
- Moriya, T. J., Sanyal, D., & Langer, N. 2015, *A&A*, 575, L10
- Nicholl, M., Berger, E., Margutti, R., et al. 2017a, *ApJL*, 835, L8
- Nicholl, M., Guillochon, J., & Berger, E. 2017b, *ApJ*, 850, 55
- Nicholl, M., & Smartt, S. J. 2016, *MNRAS*, 457, L79
- Nicholl, M., Smartt, S. J., Jerkstrand, A., et al. 2013, *Nature*, 502, 346
- Nicholl, M., Berger, E., Margutti, R., et al. 2016, *ApJL*, 828, L18
- Nomoto, K., Tanaka, M., Tominaga, N., & Maeda, K. 2010, *NewAR*, 54, 191
- Obergaulinger, M., & Aloy, M. Á. 2017, *MNRAS*, 469, L43
- Ofek, E. O., Rabinak, I., Neill, J. D., et al. 2010, *ApJ*, 724, 1396
- Owocki, S. P., & Gayley, K. G. 1997, in *Astronomical Society of the Pacific Conference Series*, Vol. 120, *Luminous Blue Variables: Massive Stars in Transition*, ed. A. Nota & H. Lamers, 121
- Paxton, B., Bildsten, L., Dotter, A., et al. 2011, *ApJS*, 192, 3
- Paxton, B., Cantiello, M., Arras, P., et al. 2013, *ApJS*, 208, 4
- Paxton, B., Marchant, P., Schwab, J., et al. 2015, *ApJS*, 220, 15
- Paxton, B., Schwab, J., Bauer, E. B., et al. 2017, ArXiv e-prints, [arXiv:1710.08424](https://arxiv.org/abs/1710.08424) [astro-ph.SR]
- Peimbert, M., Luridiana, V., & Peimbert, A. 2007, *ApJ*, 666, 636

- Pian, E., Mazzali, P. A., Masetti, N., et al. 2006, *Nature*, 442, 1011
- Podsiadlowski, P., Ivanova, N., Justham, S., & Rappaport, S. 2010, *MNRAS*, 406, 840
- Ramírez-Agudelo, O. H., Simón-Díaz, S., Sana, H., et al. 2013, *A&A*, 560, A29
- Rau, A., Kulkarni, S. R., Law, N. M., et al. 2009, *PASP*, 121, 1334
- Rembiasz, T., Guilet, J., Obergaulinger, M., et al. 2016, *MNRAS*, 460, 3316
- Schulze, S., Krühler, T., Leloudas, G., et al. 2018, *MNRAS*, 473, 1258
- Soderberg, A. M., Berger, E., Page, K. L., et al. 2008, *Nature*, 453, 469
- Sorokina, E., Blinnikov, S., Nomoto, K., Quimby, R., & Tolstov, A. 2016, *ApJ*, 829, 17
- Springmann, U. 1994, *A&A*, 289, 505
- Spruit, H. C. 2002, *A&A*, 381, 923
- Suijs, M. P. L., Langer, N., Poelarends, A.-J., et al. 2008, *A&A*, 481, L87
- Sukhbold, T., Ertl, T., Woosley, S. E., Brown, J. M., & Janka, H.-T. 2016, *ApJ*, 821, 38
- Sukhbold, T., & Woosley, S. E. 2016, *ApJL*, 820, L38
- Svirski, G., & Nakar, E. 2014, *ApJL*, 788, L14
- Szécsi, D., Langer, N., Yoon, S.-C., et al. 2015, *A&A*, 581, A15
- Takahashi, K., Yoshida, T., Umeda, H., Sumiyoshi, K., & Yamada, S. 2016, *MNRAS*, 456, 1320
- Tanaka, M., Tominaga, N., Morokuma, T., et al. 2016, *ApJ*, 819, 5
- Thompson, C., & Duncan, R. C. 1993, *ApJ*, 408, 194
- Tolstov, A., Zhiglo, A., Nomoto, K., et al. 2017, *ApJL*, 845, L2
- Usov, V. V. 1992, *Nature*, 357, 472
- van Marle, A. J., Langer, N., Yoon, S.-C., & García-Segura, G. 2008, *A&A*, 478, 769
- Vink, J. S., & de Koter, A. 2005, *A&A*, 442, 587
- Vink, J. S., de Koter, A., & Lamers, H. J. G. L. M. 2001, *A&A*, 369, 574
- Woosley, S. E. 1993, *ApJ*, 405, 273
- . 2010, *ApJL*, 719, L204
- . 2017, *ApJ*, 836, 244
- Woosley, S. E., Blinnikov, S., & Heger, A. 2007, *Nature*, 450, 390
- Woosley, S. E., & Heger, A. 2006, *ApJ*, 637, 914
- Worley, A., Krastev, P. G., & Li, B.-A. 2008, *ApJ*, 685, 390
- Yan, L., Quimby, R., Gal-Yam, A., et al. 2017, *ApJ*, 840, 57
- Yoon, S.-C., & Cantiello, M. 2010, *ApJL*, 717, L62
- Yoon, S.-C., & Langer, N. 2005, *A&A*, 443, 643
- Yoon, S.-C., Langer, N., & Norman, C. 2006, *A&A*, 460, 199
- Yoshida, T., Umeda, H., Maeda, K., & Ishii, T. 2016, *MNRAS*, 457, 351

APPENDIX

A. ADDITIONAL INFORMATION

In this section we provide additional information about our models. For Series B models, we include Fig. 13, which presents the evolution of the central densities and temperatures, Fig. 14, which complements Fig. 8 in showing the mass loss rate as a function of remaining time.

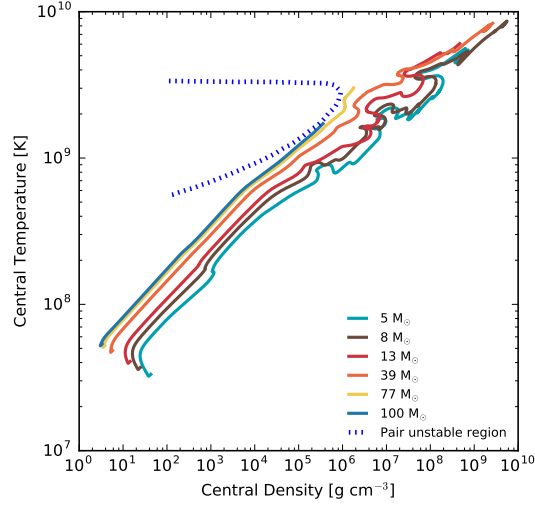


Figure 13. Central temperature versus central density evolution for Series B models of the indicated initial masses.

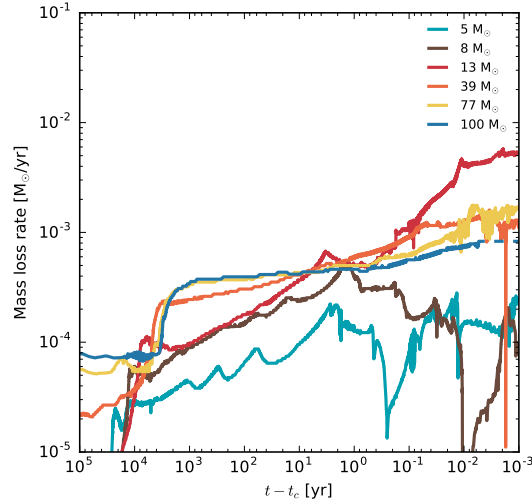


Figure 14. Mass loss rates as a function of remaining time for Series B models

Fig. 15 presents the abundances of different elements for selected pre-SN models both from Series A and Series B. For Series A, we include Tab. 2, with relevant values, complementing Tab. 1.

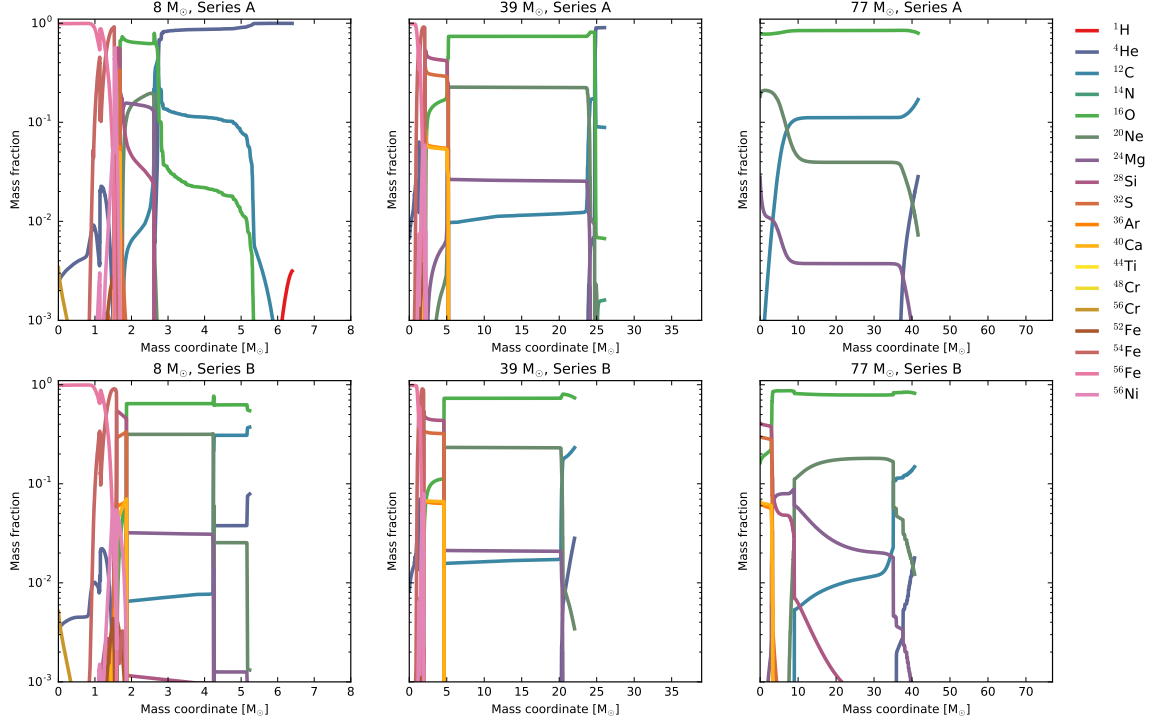


Figure 15. Mass fractions of the chemical elements as function of the Lagrangian mass coordinate in six different representative pre-SN stellar models.

Table 2. Initial and final parameters of the evolutionary sequences in Series A.

Initial mass [M_{\odot}]	5	8	13	39	77	100
Initial $\Omega/\Omega_{\text{crit}}$	0.89	0.84	0.79	0.69	0.67	0.68
CO core mass [M_{\odot}] ^a	1.43	2.63	6.06	24.80	42.66	53.51
Final mass [M_{\odot}]	4.19	6.40	9.61	26.04	41.59	52.47
$\Delta M_{\text{H}\rightarrow\text{He}}$ [M_{\odot}] ^b	0.51	0.58	1.05	4.48	13.21	19.84
$\Delta M_{\text{He}\rightarrow\text{final}}$ [M_{\odot}] ^c	0.01	0.25	0.83	1.27	1.06	1.00
f_M	0.004	0.05	0.09	0.05	0.20	0.60
Final Radius [cm]	2.38×10^{11}	1.76×10^{11}	1.34×10^{11}	3.43×10^{10}	3.90×10^{10}	4.62×10^{10}
Final T_{eff} [K]	4.85×10^4	6.86×10^4	9.52×10^4	2.12×10^5	2.86×10^5	2.84×10^5
Final H mass [M_{\odot}]	0.01	0	0	0	0	0
Final He mass [M_{\odot}]	2.32	3.33	3.19	1.16	0.05	0.07
Final Y_{surf}	0.98	1.00	0.99	0.90	0.03	0.03
Radius at $\tau = 1$ [cm]	–	–	–	9.05×10^{13}	1.61×10^{13}	1.22×10^{13}
$\bar{j}_{1.5M_{\odot}}$ [$\text{cm}^2 \text{s}^{-1}$]	2.46×10^{14}	2.83×10^{14}	8.88×10^{14}	1.88×10^{15}	5.20×10^{15}	4.48×10^{15}
$\bar{j}_{2M_{\odot}}$ [$\text{cm}^2 \text{s}^{-1}$]	8.32×10^{14}	3.57×10^{14}	8.88×10^{14}	3.72×10^{15}	6.41×10^{15}	5.73×10^{15}
$\bar{j}_{5M_{\odot}}$ [$\text{cm}^2 \text{s}^{-1}$]	–	2.73×10^{16}	3.40×10^{15}	1.12×10^{16}	1.31×10^{16}	1.15×10^{16}
P_{rot} ($1.5 M_{\odot}$ NS) [ms] ^d	19.42	16.89	5.39	2.54	0.92	1.07
E_{rot} ($1.5 M_{\odot}$ NS) [erg] ^d	1.19×10^{50}	1.57×10^{50}	1.54×10^{51}	6.93×10^{51}	5.29×10^{52}	3.92×10^{52}
Final fate	CCSN	CCSN	CCSN	CCSN	PISN	PISN

^{a–d} See Tab. 1